MODELING THE ULTRASOUND REFLECTION FROM IMMERSED LAMINATES AND ITS APPLICATION IN ADHESIVE BOND INSPECTIONS

Bernardo Feijó Junqueira

Dissertação de Mestrado apresentada ao Programa de Pós-graduação em Engenharia Mecânica, COPPE, da Universidade Federal do Rio de Janeiro, como parte dos requisitos necessários à obtenção do título de Mestre em Engenharia Mecânica.

Orientadores: Daniel Alves Castello
Ricardo Leiderman

Rio de Janeiro
Fevereiro de 2018

MODELING THE ULTRASOUND REFLECTION FROM IMMERSED LAMINATES AND ITS APPLICATION IN ADHESIVE BOND INSPECTIONS

Bernardo Feijó Junqueira

DISSERTAÇÃO SUBMETIDA AO CORPO DOCENTE DO INSTITUTO ALBERTO LUIZ COIMBRA DE PÓS-GRADUAÇÃO E PESQUISA DE ENGENHARIA (COPPE) DA UNIVERSIDADE FEDERAL DO RIO DE JANEIRO COMO PARTE DOS REQUISITOS NECESSÁRIOS PARA A OBTENÇÃO DO GRAU DE MESTRE EM CIÊNCIAS EM ENGENHARIA MECÂNICA.

Examinada por:

Prof. Daniel Alves Castello, D.Sc.

Prof. Ricardo Leiderman, D.Sc.

Prof. Fernando Augusto de Noronha Castro Pinto, D.Sc.

Prof. Gabriela Ribeiro Pereira, D.Sc.

RIO DE JANEIRO, RJ – BRASIL
FEVEREIRO DE 2018

Junqueira, Bernardo Feijó

Modeling the ultrasound reflection from immersed laminates and its application in adhesive bond inspections/Bernardo Feijó Junqueira. – Rio de Janeiro: UFRJ/COPPE, 2018.

X, 57 p.: il.; 29, 7cm.

Orientadores: Daniel Alves Castello

Ricardo Leiderman

Dissertação (mestrado) – UFRJ/COPPE/Programa de Engenharia Mecânica, 2018.

Referências Bibliográficas: p. 52 – 57.

1. Interface inspection. 2. Laminates. 3. Spring boundary conditions. 4. Invariant embedding. I. Castello, Daniel Alves *et al.* II. Universidade Federal do Rio de Janeiro, COPPE, Programa de Engenharia Mecânica. III. Título.

In memory of Bruno Feijó Junqueira, Alexandre Rodrigues Junqueira and Luiz Botelho Feijó, who accompanied my journey and are no longer here. You will always be in my heart.

Resumo da Dissertação apresentada à COPPE/UFRJ como parte dos requisitos necessários para a obtenção do grau de Mestre em Ciências (M.Sc.)

MODELAGEM DA REFLEXÃO POR ULTRASSOM DE LAMINADOS IMERSOS E SUA APLICAÇÃO EM INSPEÇÕES DE JUNTAS ADESIVAS

Bernardo Feijó Junqueira

Fevereiro/2018

Orientadores: Daniel Alves Castello
Ricardo Leiderman

Programa: Engenharia Mecânica

Este trabalho apresenta uma abordagem para a determinação do projeto ótimo de experimento para identificação de falhas em estruturas laminadas imersas em fluido acústico. As condições de contorno de mola são utilizadas para as camadas adesivas, sendo que as imperfeições nestas camadas são modeladas como uma redução das constantes elásticas das molas correspondentes. A formulação foi desenvolvida com o auxílio da técnica da imersão invariante, que é numericamente incondicionalmente estável. São identificadas as frequências/ângulos de incidência que são mais sensíveis às falhas nas juntas através da análise do coeficiente de reflexão de uma placa saudável e de uma com falha. Essas frequências/ângulos de incidência são, presumivelmente, as escolhas ideais para o campo de inspeção nas avaliações de ultrassom nas camadas adesivas.

Abstract of Dissertation presented to COPPE/UFRJ as a partial fulfillment of the requirements for the degree of Master of Science (M.Sc.)

MODELING THE ULTRASOUND REFLECTION FROM IMMERSED LAMINATES AND ITS APPLICATION IN ADHESIVE BOND INSPECTIONS

Bernardo Feijó Junqueira

February/2018

Advisors: Daniel Alves Castello
Ricardo Leiderman

Department: Mechanical Engineering

This work presents an approach for the determination of an optimal experiment design to identify faults in laminated structures immersed in acoustic fluid. The spring boundary conditions are used for the adhesive bonds and adhesion imperfections are modeled reducing the corresponding spring constants. The formulation is developed with the aid of the invariant embedding technique and, accordingly, it is numerically unconditionally stable. The frequencies/angles of incidence that are most sensitive to adhesion flaws are identified by analyzing the reflection coefficient of a healthy and a flawed plate. Such frequencies/angles of incidence are presumably the optimum choices for the inspecting field in adhesive bond ultrasound evaluations.

Contents

List of Figures

Chapter 1

Introduction

Composite materials are known by its excellent physical, mechanical and development properties. They are applied widely in aircraft technology industry (like reinforced graphite-epoxy composites), electronic engineering and recently in passenger-car technology [2]. Laminates are composed of a heterogenous combination of constituent layers and adhesive interfaces, in order to achieve an especific mix of mechanical properties, depending on its application [3]. In many cases, degradation of the thin adhesive layer, rather than of the bulk of the adherents, leads to catastrophic failure [4, 5].

Smith [6] presents a review of defects in composites. Damages on laminates can be produced during its manufacturing process or in the course of the normal service life of the component. The most common type of defect during the manufacturing is porosity, caused by incorrect cure parameters and can be critical, since this affects the mechanical properties of the joint. Other very common defect is the inclusion, as the manufacture is done by hand or machine, facilitating the entry of strange bodies. Knowing that, it is easy to assume that the distribution of the adhesive layers is most likely to be heterogeneous. In service damage is most often caused by impacts, resulting in matrix cracking and delaminations, that can cause disbonding after some period of time.

Furthermore, an application that has been attracting the attention of both academia and industrial sector is the assessment of the structural integrity of a cemented rising tube. The effective and reliable decommissioning of oil wells is a process of extreme importance for the oil industry, since any leakage is extremely harmful to the environment, in addition to causing fines for the company responsible for that well [7].

The cementation of the duct is a process used for the abandonment, which consists of placing a cement coating between the duct and the rock formation in which it is located [1], providing hydraulic insulation and ensuring that no leaks occur. The problem of this method is to ensure the integrity of the cementation, since chemical, mechanical and even operational failures can occur in the cement layer used [8], especially in the duct-cement and cement-formation interfaces.

The verification of the integrity occurs predominantly through a procedure called cement bond logging. However, this method is obsolete, and can only detect,

in a reliable way, anomalies in the interface between the duct and the cement. In most cases, this procedure is not accurate or sensitive enough to detect a flaw and other types of logging are required [9].

Moreover, Smith [6] presents the main types of non-destructive techniques to evaluate the laminate integrity:

- Ultrasonic Inspetion Methods.
- Low-frequency Vibration Methods.
- X-Radiography.
- Optical Methods.
- Thermal Methods.

1.1 Motivation

The most used and indicated method to evaluate the laminate bond interfaces is the ultrasonic inspection. As can be seen in [10–13]. This method is based on the frequency dependence of the reflected field, taking advantage of a relation between spectral minima of the reflection coefficient and the quality of the bond, proving to be very sensitive to local material flaws. Its primary disadvantage is that it requires each point of the interface to be investigated separately, determining an angle of incidence and a frequency of the incident field that are sensitive to adhesive flaws. That is, to the author's best knowledge, the implementation of a reliable non-destructive evaluation to attest the integrity of such a difficult-to-access region is still an open task. This inhibits the use of such composites in some areas in engineering.

1.2 Objective

The aim of the present work is to implement a systematic modeling technique to assist ultrasonic inspection of adhesive bonds [14, 15], generating the optimum parameters, angle of incidence and frequency, in order to calibrate the tools of the experimental procedure. This is important to evaluate composites, since its necessary to probe the bond integrity against flaws periodically.

1.3 The literature methodology

There are, basically, two approaches to simulate ultrasonic inspection of adhesive interfaces of laminates:

- Inspection using guided waves, that is used to sweep large areas and propagate lamb waves [16, 17].
- Submerged inspection, that is used to make punctual analyzes to verify the interface integrity [18].

Furthermore, the most common way to analyse the integrity of the adhesive bond is to verify when the energy is greater in the vicinity of the interface [17, 19, 20]. This is a necessary condition, but does not guarantee the sensibility to defects in the bonding interface.

1.4 The proposed methodology

A recursive algorithm was developed to calculate the reflection coefficient at the top of the laminated plate immersed in acoustic fluid. For that purpose, we "sweep" the laminate in a bottom up fashion to compute the surface impedance tensor presented to each layer. This technique is known as the invariant imbedding technique [21] and is numerically unconditionally stable even for high frequencies. Finally, the surface impedance presented in the upper fluid half-space is used to compute the reflection coefficient. Thereon, the frequencies/angles of incidence that are most sensitive to adhesion defects are identified. The problem scenario is shown in Figure 1.1.

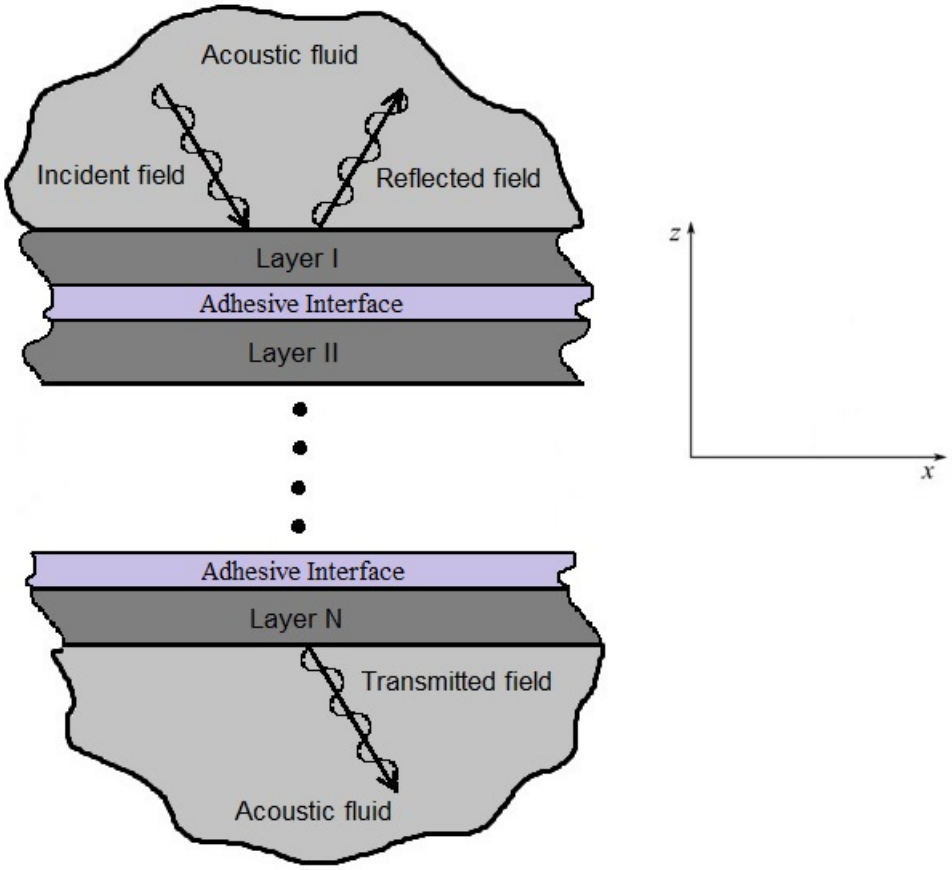

Figure 1.1: Scenario considered in the problem.

1.5 Dissertation Outline

The metodology of this work is organized as follows:

- In Chapter 2, the literature review is presented.
- In Chapter 3, section 3.1, an overview of plane waves and impedance tensors in an isotropic media is presented.
- In Chapter 3, section 3.2, an overview of plane waves and impedance tensors in an anisotropic media is presented.
- In Chapter 3, section 3.3, the mathematical formulation of the elastic layers is presented.
- In Chapter 3, section 3.4, the mathematical formulation of the adhesive layers is presented, with the aid of QSA [22].

- In Chapter 3, section 3.5, the computational procedure is explained, defining the surface impedance tensor and the reflection matrix.
- In Chapter 4, the results are presented in terms of angle of incidence and the amplitude of the reflected field.
- In Chapter 5, the conclusions are made.

Chapter 2

Literature Review

In this chapter, an overview of relevant works in the area of bonding interfaces of laminates is made. The selection is chronologically organized, in order to facilitate the visualization of all the progress achieved in this area.

In [23], Pilarski *et al.* sugests that a theoretical and quantitative solution to the problem from a non destructive evaluation point of view would be desirable in both manufacturing and for in-service investigation of a variety of different structures. Since the interface quality between layers in a laminate structure is critical in fracture and fatigue analysis.

Guo and Cawley [24] discussed the interaction of the S0 Lamb mode with delaminations, exploiting the potential of the mode to be used in long-range nondestructive inspection. A comparison of the interaction of the S0 mode with delaminations at different interfaces in a composite laminate is made, using a finite element analysis and an experimental setup. They sugest that the amplitude of the reflection of the S0 mode from a delamination is strongly dependent on the position of the delamination through the thickness of the laminate and that the delamination locations corresponding to the maximum and minimum reflectivity correspond to the locations of maximum and minimum shear stress across the interface in the S0 mode.

In [25], Singher *et al.* analyzed an acoustic wave propagation in a three-layer waveguiding configuration. They consider an adhesive layer as a waveguide structure, showing that the propagation of guided modes is affected by the bonding quality. Moreover, a comprehensive study was made by them to demonstrate the possibility of utilizing measurements on guided wave propagation to detect interfacial weakness between an adhesive and adherend.

Alleyne and Cawley [26] used a finite element analysis to investigate the interaction of individual Lamb waves with a variety of defects simulated by notches, validating experimentally the results. They have shown that a 2-D Fourier transform method may be used to quantify Lamb wave interactions with defects and that the sensitivity of individual Lamb waves to particular notches is dependent on the frequency-thickness product, the mode type and order, and the geometry of the notch. The sensitivity of some Lamb modes to simulated defects in different frequency-thickness regions is predicted as a function of the defect

depth to plate thickness ratio and the results indicate that Lamb waves may be used to find notches when the wavelength to notch depth ratio is on the order of 40. Furthermore, they show that transmission ratios of Lamb waves across defects are highly frequency dependent.

In [27], Karpur *et al.* show how critical and difficult to detect is the defect in the transversal direction of the adhesive joints, known as kissing bonds. This type of flaw is characterized when good contact exists among the adherend and the adhesive, however with no acceptable levels of adhesion, and generally is a manufactoring anomaly. With a certain period of time it can compromises the load bearing capability of the joint by initiating adhesive failure. The paper exploit the lack of a reliable method that can effectively detect a kissing bond and that the attempts to develop new methods have been unsuccessful to date.

Diamanti *et al.* [28] have considered a method of health monitoring of composites using the fundamental anti-symmetric A_0 Lamb mode [29], involving analysis of the transmitted and/or reflected wave generated by a piezoelectric device after interacting with discontinuities, testing the applicability of the technique. The materials used in this study are composite laminated carbon fibre reinforced structures. In [30], Diamanti *et al.* presented an experimental study, that demonstrates the potential of low-frequency Lamb waves being used for the inspection of monolithic and sandwich composite beams, testing multidirectional carbon fibre reinforced plastic beams of various lay ups for detection of matrix cracking, delaminations and broken fiber. Small and unobtrusive piezoceramic patches are used to generate and capture flexural waves propagating through the structure at low frequencies. The technique is also successfully applied to the damage inspection of composite sandwich beams.

In [31], Nassr and El-Dakhakhni use dielectrometry sensors to capture changes in the dieletric characteristics caused by the presence of damage in laminates. The presence of damage in the laminated composite plate leads to changes in its dielectric characteristics, causing variation in the measured capacitance by the sensors. An analytical model was used to analyse the influence of different sensor parameters on the output signals and to optimize sensor design. Two-dimensional finite element (FE) simulations were performed to assess the validity of the analytical results and to evaluate other sensor design-related parameters. To experimentally verify the model, the dielectric permittivity of the composite plate was measured. In addition, a glass fibre reinforced polymer (GFRP) laminated plate containing pre-fabricated slots through its thickness to simulate delamination and water intrusion defects was inspected in a laboratory setting. Excellent agreements were found between the experimental capacitance response signals and those predicated from the FE simulations. This cost-effective technique can be used for rapid damage screening,

regular scheduled inspection, or as a permanent sensor network within the composite system.

Amaro *et al.* [32] evaluate the features and capabilities of electronic speckle pattern interferometry (ESPI), shearography, ultrasonic testing and X-radiography when utilised to detect and quantify impact damage on composite laminates subjected to low-velocity impact. It was used a carbon fibre-reinforced epoxy composite and a drop-weight testing machine to simulate the impacts. The defects were successfully detected by all the four techniques, although the interferometric methods showed some limitations. X-radiography is an interesting alternative technique, but was not able to localize delaminations in the thickness direction. The ultrasonic methods, A-scan and C-scan, were shown to be the best solutions for inspecting the samples. According to the experimental results, these techniques were able to detect and measure the damage extent with great precision.

In [33], Ren and Lissenden exploit the advantages of ultrasonic guided waves to probe the integrity of the bonded interfaces. They were looking for a technique that is sensitive to adhesive defects without direct access to the bonded region, in order to perform a nondestructive evaluation. They take as an advantage the ability of the ultrasonic guided waves to inspect for different types of defects and travel through a structure having nonuniform cross section. Two incident modes were selected for a finite element simulation, showing that both modes have relatively large in-plane displacement at the interface and that the shear stress is near a local maximum there as well. Furthermore, experimental procedures were made, uncovering that both modes are sensitive to adhesive defects by either frequency content or amplitude ratio.

Blyth *et al.* [7] explore the applicability of logging-while-drilling (LWD) sonic tools to the analysis of cement behind casing. They consider both the currently accepted deliverable of top of cement (TOC) analysis, along with examples of more advanced processing techniques and their comparison to wireline cement evaluation, providing case study examples in each case. The use of LWD sonic tools to identify casing collar connections on driller's depth, enabling the safe positioning of cased-hole whipstocks, is also covered by them, demonstrating a novel and little-used application of LWD technology. Futhermore, they presents how the wireline acoustic tools have been used to analyze the quality of the cement bond between the casing and the formation, being developed over many years to produce high-quality assessments of cement bond, which can then be confidently used to confirm well integrity. However, the conveyance method requires that the analysis be performed on the critical path and also that additional methods be used in high-angle wells. They end up concluding that LWD technology offers a potential alternative without these issues, provided the current limitations of the

technology are understood and its applicability properly assessed as a fit-for-purpose solution. Note that there are many other works, like [1, 9, 34], that are trying to develop new and improved techniques to assist the integrity evaluation of cemented rising tubes, since it lacks of effectiveness and reliability.

In [35], Leiderman and Castello solve a similar problem with those explored in the present work by analysing a two-layer isotropic laminate adhesion interface, but formulating the resulting scattering problem as a least-squares problem. And, in [36], Leiderman *et al.* proposed an analytic-numerical method to model the interaction between guided waves and non uniform interfacial flaws in anisotropic elastic multi-layered medium. They used the QSA [22], which is addressed in the present work, to model bonding interfaces and the perturbation method due to nonuniform flaws.

Chapter 3

Mathematical Formulation

In this chapter, the transformed displacement ($\bar{\boldsymbol{u}}(k_x, z)$), stress ($\bar{\boldsymbol{\sigma}}(k_x, z)$) and traction ($\bar{\boldsymbol{t}}(k_x, z)$) are used, and can be given by:

$$\boldsymbol{u}(x, z) = \int_{-\infty}^{+\infty} \bar{\boldsymbol{u}}(k_x, z) e^{ik_x x} dk_x \tag{3.1}$$

$$\boldsymbol{\sigma}(x, z) = \int_{-\infty}^{+\infty} \bar{\boldsymbol{\sigma}}(k_x, z) e^{ik_x x} dk_x \tag{3.2}$$

$$\bar{\boldsymbol{t}} = \bar{\boldsymbol{\sigma}}.\boldsymbol{n} \tag{3.3}$$

where k_x is the x wave number and $\boldsymbol{n}$ is the unit vector normal to each interface, pointing to the positive direction of z-axis. In the equations above (and from now on), the bar over the field variables stands for a single Fourier Transform over the x direction. And the orientation of the cartesian coordinate system can be seen in Figure 3.1.

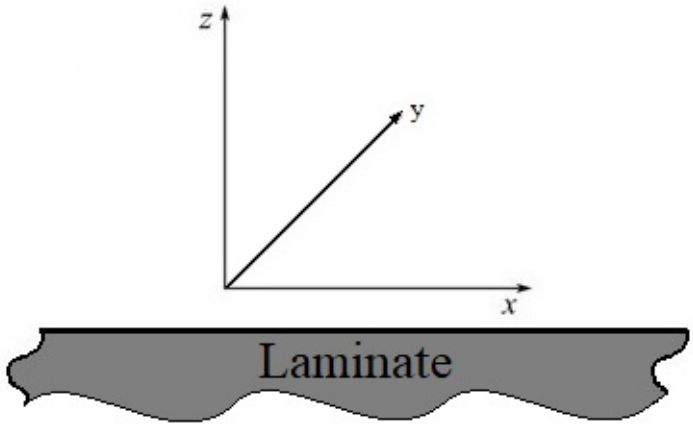

Figure 3.1: The orientation of the cartesian coordinate system.

3.1 Plane Waves and Impedance Tensors in Isotropic Media

Consider an isotropic and homogenous elastic solid medium, subjected to small deformations:

$$\tau_{\alpha\beta,\beta} + \rho f_\alpha = \rho \ddot{u}_\alpha \tag{3.4}$$

$$\tau_{\alpha\beta} = \lambda \epsilon_{kk} \delta_{\alpha\beta} + 2\mu \epsilon_{\alpha\beta} \tag{3.5}$$

$$\epsilon_{\alpha\beta} = \frac{1}{2}(u_{\alpha,\beta} + u_{\beta,\alpha}) \tag{3.6}$$

where equation (3.4) is the Newton's second law of motion applied to the continuum, known as linear momentum balance. The equation (3.5) is the constitutive relation associated to isotropic materials, better known as generalized Hooke's law. The equation (3.6) is the strain tensor related to small deformations. In the equations above, $\tau_{\alpha\beta}$ is the stress tensor, u_α is the displacement vector, ρ is the specific mass, f_α is the body force per unit mass, $\epsilon_{\alpha\beta}$ is the strain tensor and λ and μ are the Lamé parameters.

By mixing the three equations, (3.4), (3.5) and (3.6), we can write the Navier equation, which is the governing equation in terms of displacement:

$$(\lambda + \mu) u_{\beta,\beta\alpha} + \mu u_{\alpha,\beta\beta} + \rho f_\alpha = \rho \ddot{u}_\alpha \tag{3.7}$$

Or, in vector notation:

$$(\lambda + \mu) \nabla\nabla . \boldsymbol{u} + \mu \nabla^2 \boldsymbol{u} + \rho \boldsymbol{f} = \rho \ddot{\boldsymbol{u}} \tag{3.8}$$

The equation (3.7) or (3.8) is composed by three coupled scalar partial differential equations which, in Cartesian coordenates, can be written as:

$$(\lambda + \mu)\left(\frac{\partial^2 u}{\partial x^2} + \frac{\partial^2 v}{\partial x \partial y} + \frac{\partial^2 w}{\partial x \partial z}\right) + \mu\left(\frac{\partial^2 u}{\partial x^2} + \frac{\partial^2 v}{\partial y^2} + \frac{\partial^2 w}{\partial z^2}\right) + \rho f_x = \rho \frac{\partial^2 u}{\partial t^2} \tag{3.9}$$

$$(\lambda + \mu)\left(\frac{\partial^2 u}{\partial y \partial x} + \frac{\partial^2 v}{\partial y^2} + \frac{\partial^2 w}{\partial y \partial z}\right) + \mu\left(\frac{\partial^2 u}{\partial x^2} + \frac{\partial^2 v}{\partial y^2} + \frac{\partial^2 w}{\partial z^2}\right) + \rho f_y = \rho \frac{\partial^2 v}{\partial t^2} \tag{3.10}$$

$$(\lambda + \mu)\left(\frac{\partial^2 u}{\partial z \partial x} + \frac{\partial^2 v}{\partial z \partial y} + \frac{\partial^2 w}{\partial z^2}\right) + \mu\left(\frac{\partial^2 u}{\partial x^2} + \frac{\partial^2 v}{\partial y^2} + \frac{\partial^2 w}{\partial z^2}\right) + \rho f_z = \rho \frac{\partial^2 w}{\partial t^2} \tag{3.11}$$

Considering that there is no body forces:

$$\boldsymbol{f} = \begin{bmatrix} f_x & f_y & f_z \end{bmatrix}^T = 0 \tag{3.12}$$

The equation (3.7) or (3.8) can be solved with the Helmholtz decomposition, which is well explained in [37, 38]. The solution leads to a superposition of three different waves, known as primary, secondary vertical and secondary horizontal wave, that propagate uncoupled. These are called plane waves, in which all the points belonging to a plane normal to the direction of wave propagation have the same

displacement field.

3.1.1 Primary wave

The upgoing displacement field, represented by subscript "1", related to a P-wave, is given by the following expression:

$$\bar{\boldsymbol{u}}_{\boldsymbol{P_1}} = \begin{bmatrix} A\sin(\theta_1)e^{i(k_{x_1}x+k_{z_1}z-\omega t)} \\ 0 \\ A\cos(\theta_1)e^{i(k_{x_1}x+k_{z_1}z-\omega t)} \end{bmatrix} \tag{3.13}$$

And the downgoing displacement field, represented by subscript "2":

$$\bar{\boldsymbol{u}}_{\boldsymbol{P_2}} = \begin{bmatrix} D\sin(\theta_4)e^{i(k_{x_4}x-k_{z_4}z-\omega t)} \\ 0 \\ -D\cos(\theta_4)e^{i(k_{x_4}x-k_{z_4}z-\omega t)} \end{bmatrix} \tag{3.14}$$

where A and D are the waves amplitude, k_{x_α} and k_{z_α} are the projections of the wave number vector $\boldsymbol{k}$ in the x and z directions, respectively, as indicated in Figure 3.2, ω is time frequency and θ_1 and θ_4 are generic propagation angles.

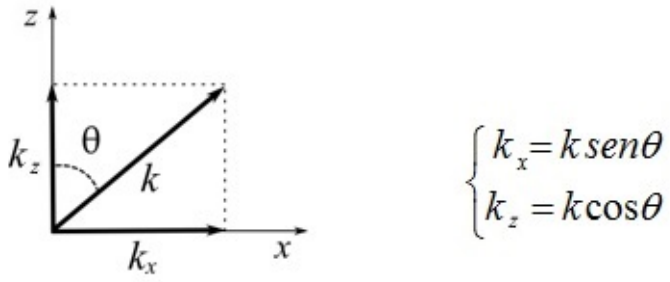

Figure 3.2: Wave number vector and its projections in the x and z directions.

The vector $\boldsymbol{k}$ always points in the direction of propagation, and the longitudinal wave number, k_L, is given by:

$$k_L = \frac{\omega}{c_L} \tag{3.15}$$

where c_L is the longitudinal propagation velocity, or the propagation velocity of P-wave, and is given by:

$$c_L = \sqrt{\frac{\lambda + 2\mu}{\rho}} \tag{3.16}$$

The P-waves have the faster propagation velocity and are known as longitudinal waves, because its displacement polarization is on the direction of the propagation of the wave, as shown in Figure 3.3.

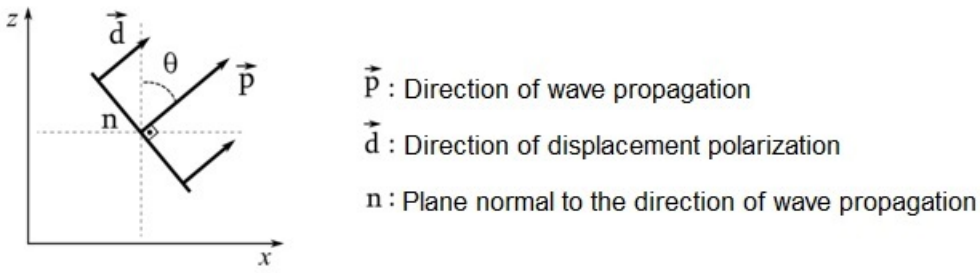

Figure 3.3: Displacement polarization of a P-wave.

P-wave is a compressive wave, because it only generates normal stresses in the direction of propagation, as shown in Figure 3.4. In this sense, these are the waves that propagate in acoustic fluids, since they do not support shear stress.

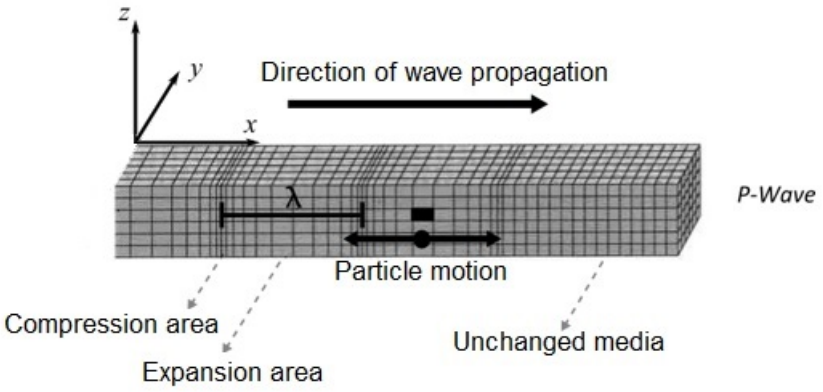

Figure 3.4: Propagation of a P-wave.

3.1.2 Secondary Vertical Wave

The upgoing displacement field, subscript "1", related to a SV-wave, is given by the following expression:

$$\bar{\boldsymbol{u}}_{\boldsymbol{SV_1}} = \begin{bmatrix} -B\cos(\theta_2)e^{i(k_{x_2}x+k_{z_2}z-\omega t)} \\ 0 \\ B\sin(\theta_2)e^{i(k_{x_2}x+k_{z_2}z-\omega t)} \end{bmatrix} \tag{3.17}$$

And the downgoing displacement field, represented by subscript "2":

$$\bar{\boldsymbol{u}}_{\boldsymbol{SV_2}} = \begin{bmatrix} E\cos(\theta_5)e^{i(k_{x_5}x - k_{z_5}z - \omega t)} \\ 0 \\ E\sin(\theta_5)e^{i(k_x x_5 - k_{z_5}z - \omega t)} \end{bmatrix} \tag{3.18}$$

where B and E are the waves amplitude, k_{x_α} and k_{z_α} are the projections of the wave number vector $\boldsymbol{k}$ in the x and z directions, respectively, ω is time frequency and θ_2 and θ_5 are generic propagation angles.

The transversal wave number, k_T, is given by:

$$k_T = \frac{\omega}{c_T} \tag{3.19}$$

where c_T is the transversal propagation velocity, or the propagation velocity of secondary wave, and is given by:

$$c_T = \sqrt{\frac{\mu}{\rho}} \tag{3.20}$$

The SV-wave propagates with a lower velocity than the P-wave, and because of this, is called secondary. They are known as transversal waves and the acronym "V" indicates that these types of waves have the displacement polarization in the plane xz, but normal to the direction of wave propagation, as shown in Figure 3.5.

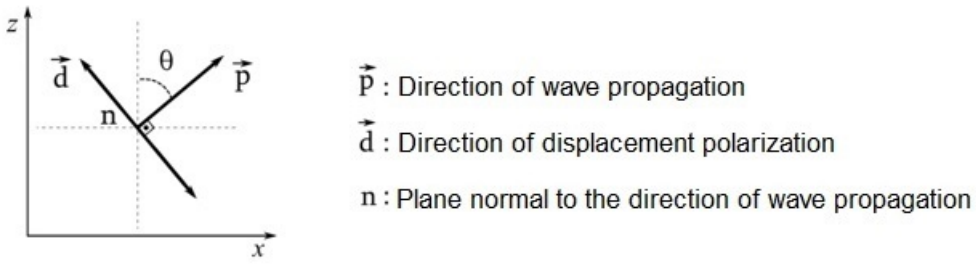

Figure 3.5: Displacement polarization of a SV-wave.

SV-wave is a shear wave, because it only generates shear stress in the direction of propagation, as shown in Figure 3.6. In this sense, these are waves that propagate only in solid media, since they only support shear stress.

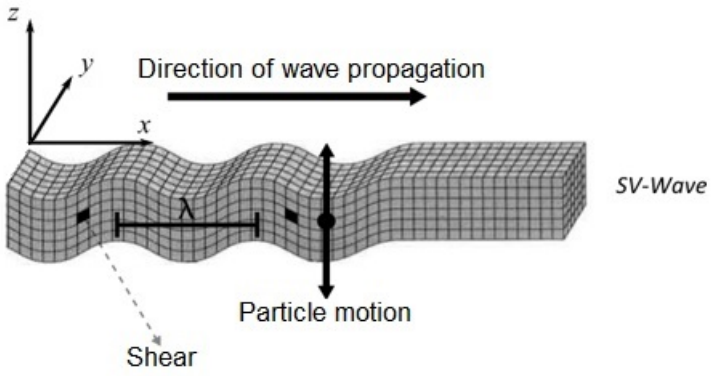

Figure 3.6: Propagation of a SV-wave.

3.1.3 Secondary Horizontal Wave

The upgoing displacement field, subscript "1", related to a SH-wave, is given by the following expression:

$$\bar{\boldsymbol{u}}_{\boldsymbol{SH_1}} = \begin{bmatrix} 0 \\ Ce^{i(k_x x_3 + k_{z_3} z - \omega t)} \\ 0 \end{bmatrix} \tag{3.21}$$

And the downgoing displacement field, represented by subscript "2":

$$\bar{\boldsymbol{u}}_{\boldsymbol{SH_2}} = \begin{bmatrix} 0 \\ Fe^{i(k_x x_6 - k_{z_6} z - \omega t)} \\ 0 \end{bmatrix} \tag{3.22}$$

where C and F are the waves amplitude, k_{x_α} and k_{z_α} are the projections of the wave number vector $\boldsymbol{k}$ in the x and z directions, respectively, and ω is time frequency.

The transversal wave number and the transversal propagation velocity are equal to SV-waves.

The SH-wave propagates with the same velocity than the SV-wave. The acronym "H" indicates that these types of waves have the displacement polarization in the y direction, normal to the direction of wave propagation, as shown in Figure 3.7.

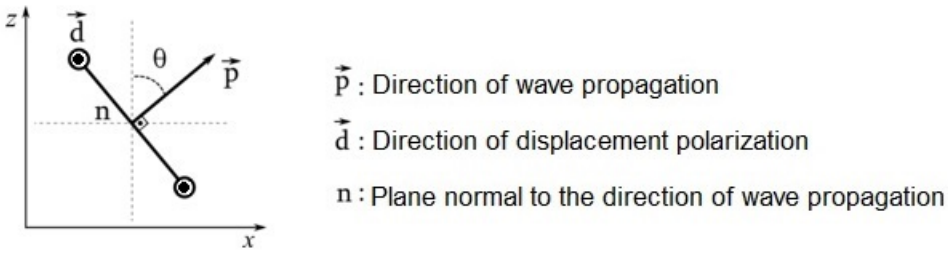

Figure 3.7: Displacement polarization of a SH-wave.

Similarly to the SV-wave, SH-wave is also a shear wave and propagates only in solid medias, but the particles motion occurs in the y-direction, as shown in Figure 3.8.

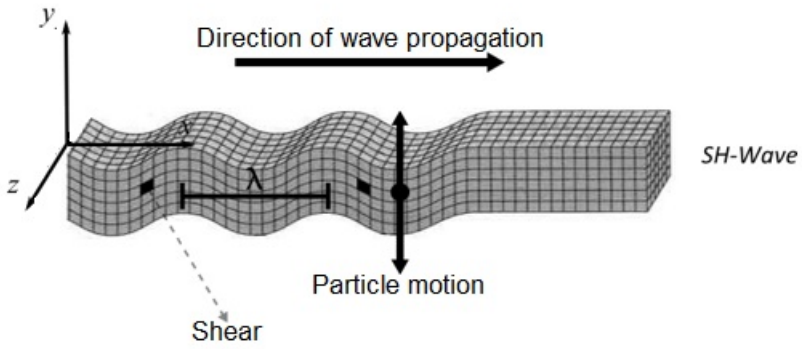

Figure 3.8: Propagation of a SH-wave.

3.1.4 Impedance Tensor and Matrix M in an Isotropic Media

Now that we know that plane waves are given by the superposition of P, SV and SH waves, suppose that we have two plane waves propagating up and down the z direction and that we are solving the problem in the time frequency domain. Assuming x=0, since we are only interested in propagation on the z-axis. These assumptions lead to the following up- and downgoing displacement vectors:

$$\bar{\boldsymbol{u}}_{\mathbf{1}} = \bar{\boldsymbol{u}}_{\boldsymbol{P_1}} + \bar{\boldsymbol{u}}_{\boldsymbol{SV_1}} + \bar{\boldsymbol{u}}_{\boldsymbol{SH_1}} = \begin{bmatrix} A\sin(\theta_1)e^{ik_{z_1}z} - B\cos(\theta_2)e^{ik_{z_2}z} \\ Ce^{ik_{z_3}z} \\ A\cos(\theta_1)e^{ik_{z_1}z} + B\sin(\theta_2)e^{ik_{z_2}z} \end{bmatrix} \tag{3.23}$$

$$\bar{\boldsymbol{u}}_{\mathbf{2}} = \bar{\boldsymbol{u}}_{\boldsymbol{P_2}} + \bar{\boldsymbol{u}}_{\boldsymbol{SV_2}} + \bar{\boldsymbol{u}}_{\boldsymbol{SH_2}} = \begin{bmatrix} D\sin(\theta_4)e^{-ik_{z_4}z} + E\cos(\theta_5)e^{-ik_{z_5}z} \\ Fe^{-ik_{z_6}z} \\ -D\cos(\theta_4)e^{-ik_{z_4}z} + E\sin(\theta_5)e^{-ik_{z_5}z} \end{bmatrix} \tag{3.24}$$

And computing the traction vectors by equations (3.5) and (3.6), we have:

$$\bar{\boldsymbol{t}}_{\boldsymbol{1}} = \bar{\boldsymbol{t}}_{\boldsymbol{P_1}} + \bar{\boldsymbol{t}}_{\boldsymbol{SV_1}} + \bar{\boldsymbol{t}}_{\boldsymbol{SH_1}} \tag{3.25}$$

$$\bar{\boldsymbol{t}}_{\boldsymbol{1_x}} = i\mu(A\sin(\theta_1)k_{z1}e^{ik_{z_1}z} + A\cos(\theta_1)k_x e^{ik_{z_1}z} - B\cos(\theta_2)k_{z2}e^{ik_{z_2}z} + B\sin(\theta_2)k_x e^{ik_{z_2}z}) \tag{3.26}$$

$$\bar{\boldsymbol{t}}_{\boldsymbol{1_y}} = i\mu C k_{z3} e^{ik_{z_3}z} \tag{3.27}$$

$$\begin{aligned}\bar{\boldsymbol{t}}_{\boldsymbol{1_z}} = i\lambda(A\sin(\theta_1)k_x e^{ik_{z_1}z} + A\cos(\theta_1)k_{z1}e^{ik_{z_1}z} - B\cos(\theta_2)k_x e^{ik_{z_2}z} + B\sin(\theta_2)k_{z2}e^{ik_{z_2}z}) \\ +2i\mu(A\cos(\theta_1)k_{z1}e^{ik_{z_1}z} + B\sin(\theta_2)k_{z2}e^{ik_{z_2}z})\end{aligned} \tag{3.28}$$

$$\bar{\boldsymbol{t}}_{\boldsymbol{2}} = \bar{\boldsymbol{t}}_{\boldsymbol{P_2}} + \bar{\boldsymbol{t}}_{\boldsymbol{SV_2}} + \bar{\boldsymbol{t}}_{\boldsymbol{SH_2}} \tag{3.29}$$

$$\bar{\boldsymbol{t}}_{\boldsymbol{2_x}} = i\mu(-D\sin(\theta_4)k_{z4}e^{-ik_{z_4}z} - D\cos(\theta_4)k_x e^{-ik_{z_4}z} - E\cos(\theta_5)k_{z5}e^{-ik_{z_5}z} + E\sin(\theta_5)k_x e^{-ik_{z_5}z}) \tag{3.30}$$

$$\bar{\boldsymbol{t}}_{\boldsymbol{2_y}} = -i\mu F k_{z6} e^{-ik_{z_6}z} \tag{3.31}$$

$$\begin{aligned}\bar{\boldsymbol{t}}_{\boldsymbol{2_z}} = \lambda(D\sin(\theta_4)k_x e^{-ik_{z_4}z} + D\cos(\theta_4)k_{z4}e^{-ik_{z_4}z} + E\cos(\theta_5)k_x e^{-ik_{z_5}z} - E\sin(\theta_5)k_{z5}e^{-ik_{z_5}z}) \\ +2i\mu(D\cos(\theta_4)k_{z4}e^{-ik_{z_4}z} - E\sin(\theta_5)k_{z5}e^{-ik_{z_5}z})\end{aligned} \tag{3.32}$$

These vectors can be rewritten in a decomposition of matrices:

$$\bar{\boldsymbol{u}}_{\boldsymbol{\alpha}}(z) = \boldsymbol{A}_{\boldsymbol{\alpha}}\boldsymbol{\Phi}_{\boldsymbol{\alpha}}(z)\boldsymbol{C}_{\boldsymbol{\alpha}}, \quad \alpha = 1, 2 \tag{3.33}$$

$$\bar{\boldsymbol{t}}_{\boldsymbol{\alpha}}(z) = -i\boldsymbol{L}_{\boldsymbol{\alpha}}\boldsymbol{\Phi}_{\boldsymbol{\alpha}}(z)\boldsymbol{C}_{\boldsymbol{\alpha}}, \quad \alpha = 1, 2 \tag{3.34}$$

where C_1 and C_2 are the amplitude vectors:

$$\boldsymbol{C_1} = \begin{bmatrix} A \\ B \\ C \end{bmatrix} \tag{3.35}$$

$$\boldsymbol{C_2} = \begin{bmatrix} D \\ E \\ F \end{bmatrix} \tag{3.36}$$

And the operators $\boldsymbol{A_1}$, $\boldsymbol{A_2}$,$\boldsymbol{L_1}$, $\boldsymbol{L_2}$ $\boldsymbol{\Phi_1}(z)$ and $\boldsymbol{\Phi_1}(z)$ are given by:

$$\boldsymbol{A_1} = \begin{bmatrix} \sin(\theta_1) & -\cos(\theta_2) & 0 \\ 0 & 0 & 1 \\ \cos(\theta_1) & \sin(\theta_2) & 0 \end{bmatrix} \tag{3.37}$$

$$\boldsymbol{A_2} = \begin{bmatrix} \sin(\theta_4) & \cos(\theta_5) & 0 \\ 0 & 0 & 1 \\ -\cos(\theta_4) & \sin(\theta_5) & 0 \end{bmatrix} \tag{3.38}$$

$$\boldsymbol{L_1} = \begin{bmatrix} -\mu(\sin(\theta_1)k_{z_1} + \cos\theta_1 k_x) & \mu(\cos(\theta_2)k_{z_2} - \sin(\theta_2)k_x) & 0 \\ 0 & 0 & -\mu k_{z_3} \\ -\lambda(\cos(\theta_1)k_{z_1} + \sin(\theta_1)k_x) - 2\mu\cos(\theta_1)k_{z_1} & \lambda(-\sin(\theta_2)k_{z_2} + \cos(\theta_2)k_x) - 2\mu\sin(\theta_2)k_{z_2} & 0 \end{bmatrix} \tag{3.39}$$

$$\boldsymbol{L_2} = \begin{bmatrix} \mu(\sin(\theta_4)k_{z_4} + \cos\theta_4 k_x) & \mu(\cos(\theta_5)k_{z_5} - \sin(\theta_5)k_x) & 0 \\ 0 & 0 & \mu k_{z_6} \\ -\lambda(\cos(\theta_4)k_{z_4} + \sin(\theta_4)k_x) - 2\mu\cos(\theta_4)k_{z_4} & \lambda(-\sin(\theta_5)k_{z_5} + \cos(\theta_5)k_x) + 2\mu\sin(\theta_5)k_{z_5} & 0 \end{bmatrix} \tag{3.40}$$

$$\boldsymbol{\Phi_1}(z) = \begin{bmatrix} e^{ik_{z_1}z} & 0 & 0 \\ 0 & e^{ik_{z_2}z} & 0 \\ 0 & 0 & e^{ik_{z_3}z} \end{bmatrix} \tag{3.41}$$

$$\boldsymbol{\Phi_2}(z) = \begin{bmatrix} e^{-ik_{z_4}z} & 0 & 0 \\ 0 & e^{-ik_{z_5}z} & 0 \\ 0 & 0 & e^{-ik_{z_6}z} \end{bmatrix} \tag{3.42}$$

The displacement and traction vectors can also be written as a function of the matrix operators $\boldsymbol{M_1}(z)$, $\boldsymbol{M_2}(z)$, $\boldsymbol{Z_1}$, $\boldsymbol{Z_2}$.

$$\bar{\boldsymbol{u}}_{\boldsymbol{\alpha}}(z) = \boldsymbol{M_\alpha}(z)\bar{\boldsymbol{u}}_{\boldsymbol{\alpha}}(0), \alpha = 1, 2 \tag{3.43}$$

$$\bar{\boldsymbol{t}}_{\boldsymbol{\alpha}}(z) = -i\omega \boldsymbol{Z_\alpha}\bar{\boldsymbol{u}}_{\boldsymbol{\alpha}}(z), \quad \alpha = 1, 2 \tag{3.44}$$

where $\boldsymbol{M_1}(z)$ and $\boldsymbol{M_2}(z)$ propagate, respectively, the up- and downgoing displacement fields in the solid. The operators $\boldsymbol{Z_1}$ and $\boldsymbol{Z_2}$ are the impedance tensors, which relate the tractions to the displacement fields and depend only on the material. These operators can be computed as:

$$\boldsymbol{M_\alpha}(z) = \boldsymbol{A_\alpha}.\boldsymbol{\Phi_\alpha}(z).[\boldsymbol{A_\alpha}]^{-1}, \quad \alpha = 1, 2 \tag{3.45}$$

$$\boldsymbol{Z_\alpha} = \frac{1}{\omega}\boldsymbol{L_\alpha}.[\boldsymbol{A_\alpha}]^{-1}, \quad \alpha = 1, 2 \tag{3.46}$$

3.2 Plane Waves and Impedance Tensors in Anisotropic Media

3.2.1 Christoffel equation

Consider an anisotropic and elastic solid medium, subjected to small deformations:

$$\tau_{ij,j} = \rho \ddot{U}_i \tag{3.47}$$

$$\tau_{ij} = C_{ijkl}\epsilon_{kl} \tag{3.48}$$

$$\epsilon_{kl} = \frac{1}{2}(U_{k,l} + U_{l,k}) \tag{3.49}$$

where equation (3.47) is the Newton's second law of motion applied to the continuum, with no body forces, known as linear momentum balance. The equation (3.48) is the constitutive relation associated to anisotropic materials, better known as generalized Hooke's law. The equation (3.49) is the strain tensor related to small deformations. In the equations above, τ_{ij} is the stress tensor, U_i is the displacement vector, ρ is the specific mass, C_{ijkl} is the stiffness tensor and ϵ_{kl} is the strain tensor.

By mixing the three equations, (3.47), (3.48) and (3.49), we can write the governing equation in terms of displacement:

$$\frac{1}{2}C_{ijkl}\left(U_{k,jl} + U_{l,jk}\right) = \rho \ddot{U}_i \tag{3.50}$$

Note that C_{ijkl} is symmetrical with respect to k and l and therefore k and l are interchangeable. This reduces the total number of stiffness parameters from 81 to 36:

$$C_{ijkl} = C_{jikl} = C_{ijlk} \tag{3.51}$$

$$\frac{1}{2}C_{ijkl}\left(U_{k,jl} + U_{l,jk}\right) = C_{ijkl}U_{l,jk} \tag{3.52}$$

Through this symmetry, the stiffness tensor can be written as a 6×6 matrix, where:

$$C_{ijkl} \rightarrow C_{nm}\,; \quad n = 1, ..., 6 \;\; and \;\; m = 1, ..., 6 \tag{3.53}$$

$$If \;\; i = j \;:\; n = i; \quad If \;\; i \neq j \;:\; n = 9 - (i + j) \tag{3.54}$$

$$If \;\; k = l \;:\; m = k; \quad If \;\; k \neq l \;:\; m = 9 - (k + l) \tag{3.55}$$

This representation of the stiffness tensor is extremely useful for some applications. Let's assume harmonic plane waves as a candidate for solution:

$$U_i = A_i e^{i(k_j x_j - \omega t)} \tag{3.56}$$

where ω is the time frequency, k_j is the wave number in the j direction, and the second time derivative can be written as:

$$\ddot{U}_i = \omega^2 U_i \tag{3.57}$$

And the spatial derivatives:

$$U_{l,jk} = k_j k_k U_l \tag{3.58}$$

Then the Christoffel equation for anisotropic media can be written by replacing the equations (3.57) and (3.58) into (3.50):

$$(\rho\omega^2\delta_{il} - C_{ijkl}k_j k_k)U_l = 0 \tag{3.59}$$

And the Christoffel acoustic tensor is given by:

$$\Lambda_{il} = C_{ijkl}n_j n_k \tag{3.60}$$

where n_j and n_k are direction cosines of the normal to the wavefront.

And finally, mixing the equations (3.59), (3.60) and the relation $k = \omega/c$ leads to a classic eigenvalue-eigenvector problem, providing us three homogeneous equations, three real roots and three distinct velocities:

$$(\Lambda_{il} - \rho c^2\delta_{il})U_l = 0 \tag{3.61}$$

3.2.2 Impedance Tensor and Matrix M in an Anisotropic Media

Taking into account the equation (2.49) and taking as a solution plane waves harmonic in time that have the xz plane as a propagation plane, one can write:

$$\boldsymbol{U}(x, z, t) = \boldsymbol{u}(x, z)e^{-i\omega t} \tag{3.62}$$

$$\boldsymbol{T}(x, z, t) = \boldsymbol{t}(x, z)e^{-i\omega t} \tag{3.63}$$

where the displacement vector $\boldsymbol{u}$ and the traction vector $\boldsymbol{t}$ have the form:

$$\boldsymbol{u} = \begin{bmatrix} u \\ v \\ w \end{bmatrix} \tag{3.64}$$

$$\boldsymbol{t} = \begin{bmatrix} \tau_{zx} \\ \tau_{zy} \\ \tau_{zz} \end{bmatrix} \tag{3.65}$$

And the state vector can be defined as:

$$\boldsymbol{\xi} = \begin{bmatrix} \boldsymbol{u}(z, k_x) \\ i\boldsymbol{t}(z, k_x) \end{bmatrix} \tag{3.66}$$

where k_x is the wave number in the x direction.

From the definition of the equations (3.62) and (3.63), the equation (3.49) and using the Fourier transform in the state vector, it can be shown that:

$$\frac{\partial}{\partial z}\bar{\boldsymbol{\xi}}(z, k_x) = i\hat{\boldsymbol{N}}(k_x)\bar{\boldsymbol{\xi}}(z, k_x) \tag{3.67}$$

where $\hat{\boldsymbol{N}}$ is the transformed of the sixth order state matrix, defined by equation (3.68), while the time dependence is canceled by appearing on both sides of the equation.

$$\hat{\boldsymbol{N}}(k_x) = \begin{bmatrix} -k_x \boldsymbol{X2}^{-1}\boldsymbol{X1} & -\boldsymbol{X2}^{-1} \\ -\omega^2\rho\boldsymbol{I} + k_x^2\boldsymbol{Y1} - k_x^2\boldsymbol{Y2}\boldsymbol{X2}^{-1}\boldsymbol{X1} & -k_x\boldsymbol{Y2}\boldsymbol{X2}^{-1} \end{bmatrix} \tag{3.68}$$

And the $\boldsymbol{X1}$, $\boldsymbol{X2}$, $\boldsymbol{Y1}$ and $\boldsymbol{Y2}$ operators are represented by the following matrices:

$$\boldsymbol{X1} = \begin{bmatrix} C_{51} & C_{56} & C_{55} \\ C_{41} & C_{46} & C_{45} \\ C_{31} & C_{36} & C_{35} \end{bmatrix} \tag{3.69}$$

$$\boldsymbol{X2} = \begin{bmatrix} C_{55} & C_{54} & C_{53} \\ C_{45} & C_{44} & C_{43} \\ C_{35} & C_{34} & C_{33} \end{bmatrix} \tag{3.70}$$

$$\boldsymbol{Y1} = \begin{bmatrix} C_{11} & C_{16} & C_{15} \\ C_{61} & C_{66} & C_{65} \\ C_{51} & C_{56} & C_{55} \end{bmatrix} \tag{3.71}$$

$$\boldsymbol{Y2} = \begin{bmatrix} C_{15} & C_{14} & C_{13} \\ C_{65} & C_{64} & C_{63} \\ C_{55} & C_{54} & C_{53} \end{bmatrix} \tag{3.72}$$

The state matrix $\hat{\boldsymbol{N}}$ has an important role in calculating the impedance tensors, since its eigenvalues represent the k_{zi} wave numbers and its eigenvectors represent the polarization vectors related to the uncoupled waves propagating inside the medium. Due to the state matrix properties, the eigenvalues appears in pairs with opposite signs, dividing in groups of three upgoing (positive direction of z-axis) and three downgoing (negative direction of z-axis) waves. Furthermore, it is important to note that this approach satisfies the Christoffel equation.

Similarly to the isotropic case, the propagation matrices $\boldsymbol{M_\alpha}$ and impedance tensors $\boldsymbol{Z_\alpha}$ are calculated as follows:

$$\boldsymbol{M_\alpha}(z) = \boldsymbol{A_\alpha}.\boldsymbol{\Phi_\alpha}(z).[\boldsymbol{A_\alpha}]^{-1}, \alpha = 1,2 \tag{3.73}$$

$$\boldsymbol{Z_\alpha} = \frac{1}{\omega}\boldsymbol{L_\alpha}.[\boldsymbol{A_\alpha}]^{-1}, \alpha = 1,2 \tag{3.74}$$

And the operators $\boldsymbol{\Phi_\alpha}$, $\boldsymbol{A_\alpha}$ and $\boldsymbol{L_\alpha}$ are calculated through the eigenvalues and eigenvectors (k_{zi} and $\boldsymbol{v_i}$) of the state matrix $\hat{\boldsymbol{N}}$, where the subscripts 1,2 and 3 refers to upgoing waves and 4, 5 and 6 refers to downgoing waves.

$$\boldsymbol{\Lambda}_{\hat{\boldsymbol{N}}} = \begin{bmatrix} k_{z1} & 0 & 0 & 0 & 0 & 0 \\ 0 & k_{z2} & 0 & 0 & 0 & 0 \\ 0 & 0 & k_{z3} & 0 & 0 & 0 \\ 0 & 0 & 0 & k_{z4} & 0 & 0 \\ 0 & 0 & 0 & 0 & k_{z5} & 0 \\ 0 & 0 & 0 & 0 & 0 & k_{z6} \end{bmatrix} \tag{3.75}$$

$$\boldsymbol{V}_{\hat{\boldsymbol{N}}} = \begin{bmatrix} \boldsymbol{v_1} & \boldsymbol{v_2} & \boldsymbol{v_3} & \boldsymbol{v_4} & \boldsymbol{v_5} & \boldsymbol{v_6} \end{bmatrix} = \begin{bmatrix} a1_{11} & a1_{12} & a1_{13} & a2_{11} & a2_{12} & a2_{13} \\ a1_{21} & a1_{22} & a1_{23} & a2_{21} & a2_{22} & a2_{23} \\ a1_{31} & a1_{32} & a1_{33} & a2_{31} & a2_{32} & a2_{33} \\ l1_{11} & l1_{12} & l1_{13} & l2_{11} & l2_{12} & l2_{13} \\ l1_{21} & l1_{22} & l1_{23} & l2_{21} & l2_{22} & l2_{23} \\ l1_{31} & l1_{32} & l1_{33} & l2_{31} & l2_{32} & l2_{33} \end{bmatrix} \tag{3.76}$$

$$\boldsymbol{\Phi_1} = \begin{bmatrix} e^{ik_{z1}z} & 0 & 0 \\ 0 & e^{ik_{z2}z} & 0 \\ 0 & 0 & e^{ik_{z3}z} \end{bmatrix} \tag{3.77}$$

$$\boldsymbol{\Phi_2} = \begin{bmatrix} e^{ik_{z4}z} & 0 & 0 \\ 0 & e^{ik_{z5}z} & 0 \\ 0 & 0 & e^{ik_{z6}z} \end{bmatrix} \tag{3.78}$$

$$\boldsymbol{A_1} = \begin{bmatrix} a1_{11} & a1_{12} & a1_{13} \\ a1_{21} & a1_{22} & a1_{23} \\ a1_{31} & a1_{32} & a1_{33} \end{bmatrix} \tag{3.79}$$

$$\boldsymbol{A_2} = \begin{bmatrix} a2_{11} & a2_{12} & a2_{13} \\ a2_{21} & a2_{22} & a2_{23} \\ a2_{31} & a2_{32} & a2_{33} \end{bmatrix} \tag{3.80}$$

$$\boldsymbol{L_1} = \begin{bmatrix} l1_{11} & l1_{12} & l1_{13} \\ l1_{21} & l1_{22} & l1_{23} \\ l1_{31} & l1_{32} & l1_{33} \end{bmatrix} \tag{3.81}$$

$$\boldsymbol{L_2} = \begin{bmatrix} l2_{11} & l2_{12} & l2_{13} \\ l2_{21} & l2_{22} & l2_{23} \\ l2_{31} & l2_{32} & l2_{33} \end{bmatrix} \tag{3.82}$$

Further details and the definitions for $\boldsymbol{M_j}(z)$ and $\boldsymbol{Z_j}$ for isotropic and anisotropic medium can be found in [39, 40].

3.3 Elastic Layers

It is assumed that the wave fields are time harmonic and, therefore, satisfy the following equations for stress $\boldsymbol{\sigma}$ and displacement $\boldsymbol{u}$ in solid layers [29]:

$$\nabla \boldsymbol{\sigma} + \rho\omega^2 \boldsymbol{u} = 0 \tag{3.83}$$

$$\boldsymbol{\sigma} = \boldsymbol{C} : \nabla \boldsymbol{u} \tag{3.84}$$

where $\boldsymbol{C}$ is the elasticity tensor, ρ is specific mass and ω is the angular frequency in rad/s. $\boldsymbol{C}$ and ρ may vary from layer to layer. In addition, layers may be either isotropic or anisotropic. This formulation is made with the aid of the invariant embedding technique [21]. Accordingly, the displacement $\boldsymbol{u}$ and traction $\boldsymbol{t}$, which will be discussed further, were decomposed into upgoing and downgoing fields.

$$\boldsymbol{u} = \boldsymbol{u}_1 + \boldsymbol{u}_2 \tag{3.85}$$

$$\boldsymbol{t} = \boldsymbol{t}_1 + \boldsymbol{t}_2 \tag{3.86}$$

where the subscript 1 is associated to upgoing fields, i.e., fields propagating (or being attenuated) in the positive vertical (z) direction, while the subscript 2 is associated to downgoing fields, i.e., fields propagating (or being attenuated) in the negative vertical (z) direction. From the exact solution of the elastodynamic equations of motion, the 3 x 3 matrix operators $\boldsymbol{M_1}(z)$, $\boldsymbol{M_2}(z)$, $\boldsymbol{Z_1}$ and $\boldsymbol{Z_2}$ are determined. The operators $\boldsymbol{M_1}(z)$ and $\boldsymbol{M_2}(z)$ propagate the up and downgoing displacement fields within each layer:

$$\bar{\boldsymbol{u}}_{\boldsymbol{j}}(z_2) = \boldsymbol{M_j}(z_2 - z_1)\bar{\boldsymbol{u}}_{\boldsymbol{j}}(z_1), j = 1, 2 \tag{3.87}$$

where z_1 and z_2 are the $z - axis$ coordenates of the beggining and the end of a layer, respectively, and, therefore, $z_1 - z_2$ is the layer thickness. Furthermore, the local impedance tensors $\boldsymbol{Z_1}$ and $\boldsymbol{Z_2}$, in turn, relate the up and downgoing traction vectors to the respective displacement fields:

$$\bar{\boldsymbol{t}}_{\boldsymbol{j}} = -i\omega \boldsymbol{Z_j} \bar{\boldsymbol{u}}_{\boldsymbol{j}}, j = 1, 2 \tag{3.88}$$

3.4 Adhesive Layers

The adhesive bonds can be treated as a layer of infinitesimal thickness, by a continuous distribution of normal and transversal springs, that connects the elastic layers, enforce continuity of traction and, approximately, displacement fields, as shown in Figure 3.9. This is called the Quasi-Static Approximation (QSA), introduced by Baik and Thompson in [22], and is an extremely used approach, as can be seen in [10, 11, 27, 41–45]. This approach is valid for inspecting wavelengths larger than the layer thickness.

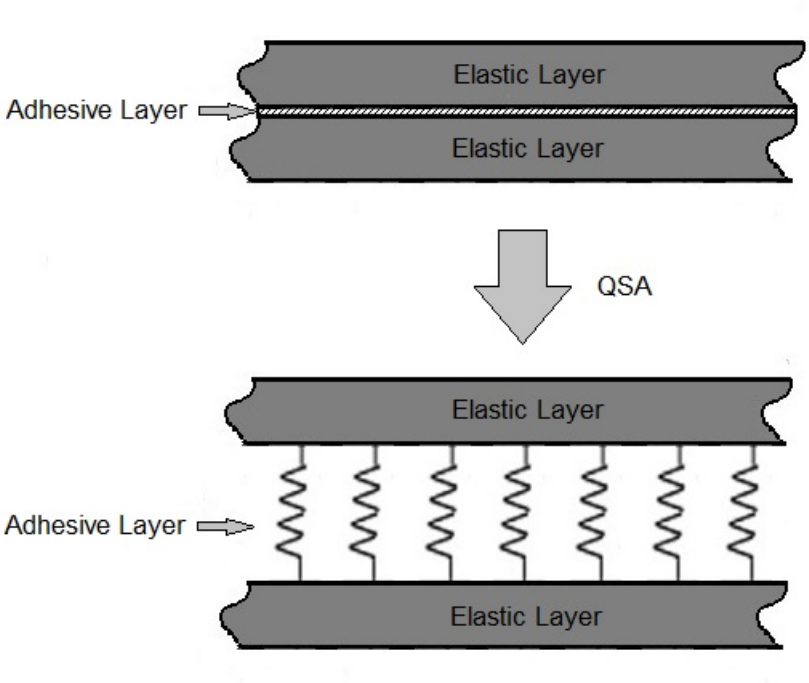

Figure 3.9: The QSA, schematically represented.

It gives us the following spring boundary conditions:

$$\boldsymbol{K}[\boldsymbol{u}^{+} - \boldsymbol{u}^{-}] = \boldsymbol{t}^{+} \tag{3.89}$$

$$\boldsymbol{t}^{-} = \boldsymbol{t}^{+} \tag{3.90}$$

the superscript "+" indicates the values of the field variables immediately above the adhesive interface, while the superscript "-" indicates those immediately below, as follows in Figure 3.10:

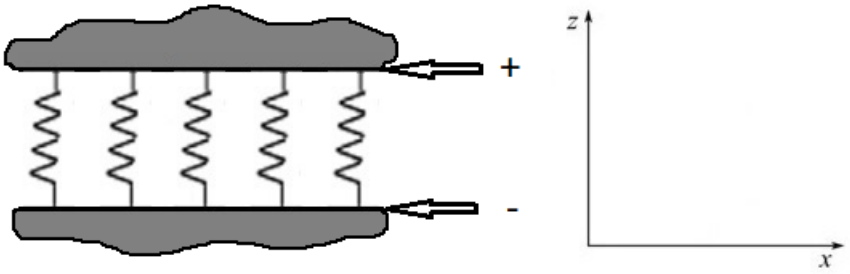

Figure 3.10: Representation of the field variables immediately above and bellow the adhesive interface.

$\boldsymbol{K}$ is a 3 x 3 diagonal spring matrix representing the effective interfacial stiffness and whose entries are normal and tangential spring constants, described as follows:

$$\boldsymbol{K} = \begin{bmatrix} K_{xx} & 0 & 0 \\ 0 & K_{yy} & 0 \\ 0 & 0 & K_{zz} \end{bmatrix} \tag{3.91}$$

It is important to note that this spring matrix has no crossed terms. This comes from the QSA, which does not use spring coupling in its approach.

Since its introduction, the QSA has been extensively used in theoretical works to model adhesive bonds and rough contact interfaces between solids (See, e.g., [10, 11, 27, 41–45]). The precise values of $\boldsymbol{K}$ can be written in terms of the elastic properties and nominal thickness of the considered interfacial layer [44]:

$$S_{int} = \frac{1}{\mu_{int}}; \tag{3.92}$$

$$C_{int} = 2\mu_{int} + \lambda_{int}; \tag{3.93}$$

$$\boldsymbol{K} = \left(h_{int} \times \begin{bmatrix} S_{int} & 0 & 0 \\ 0 & S_{int} & 0 \\ 0 & 0 & 1/C_{int} \end{bmatrix} \right)^{-1} \tag{3.94}$$

where μ_{int} and λ_{int} are the lamé parameters of the interfacial layer and h_{int} is its thickness.

Higher order extension of similar model for thin layer has been recently described in [46] and [47]. In the context of the QSA, defective bonds are usually modeled by a reduction in the spring constants (see, e.g., [48]).

3.5 Computational Procedure

In this section a recursive algorithm is presented to compute the reflection coefficient at the top of a laminate immersed in an acoustic fluid. To that end, it is desired to work with the surface impedance tensors of the solid. More specifically, the layered structure is swept in a bottom up fashion, computing the surface impedance tensor $\boldsymbol{G}$ presented to each layer, as schematically depicted in Figure 3.11.

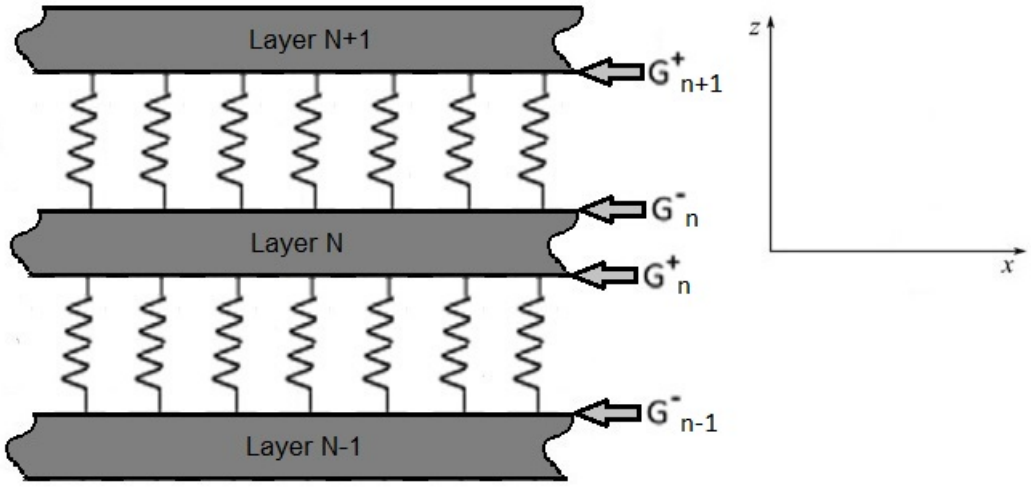

Figure 3.11: Surface impedance tensor calculation scheme, where G^+ is the impedance tensor immediately above the interface and G^- immediately bellow.

This entire process presented bellow is known as the invariant embbeded technique [21, 36, 40]. The surface impedance tensor is defined through the relation:

$$\bar{\boldsymbol{t}} = -i\omega \boldsymbol{G} \bar{\boldsymbol{u}} \tag{3.95}$$

In the sense of what is said above, the first step consists of the computation of the surface impedance at the bottom of the laminate. For an acoustic fluid half-space in which the radiation condition is satisfied at infinity, $\boldsymbol{G} = \boldsymbol{Z_f}$, where $\boldsymbol{Z_f}$ is the fluid local impedance tensor:

$$\boldsymbol{Z_f} = \begin{bmatrix} 0 & 0 & 0 \\ 0 & 0 & 0 \\ 0 & 0 & Z_f \end{bmatrix} \tag{3.96}$$

$$Z_f = \frac{\rho_f \omega}{\gamma} \tag{3.97}$$

Since ρ_f is the fluid density and γ is the fluid wave number in the z (vertical) direction.

At this point, the reflection matrix $\boldsymbol{R}$ that relates the downgoing to the upgoing displacement at the first layer's bottom is introduced, so that:

$$\bar{\boldsymbol{u}}_{\mathbf{1}} = \boldsymbol{R}\bar{\boldsymbol{u}}_{\mathbf{2}} \tag{3.98}$$

solving for $\boldsymbol{R}$ we get:

$$\boldsymbol{R} = (\boldsymbol{G} - \boldsymbol{Z}_{\mathbf{1}})^{-1}(\boldsymbol{Z}_{\mathbf{2}} - \boldsymbol{G}) \tag{3.99}$$

where $\boldsymbol{Z}_{\mathbf{1}}$ and $\boldsymbol{Z}_{\mathbf{2}}$ are the up and downgoing local impedance tensors associated to the solid, respectively.

In the next step, the surface impedance tensor at the top of the first elastic layer is computed:

$$\boldsymbol{G} = [\boldsymbol{Z}_{\mathbf{1}}\boldsymbol{P} + \boldsymbol{Z}_{\mathbf{2}}][\boldsymbol{P} + \boldsymbol{I}]^{-1} \tag{3.100}$$

where

$$\boldsymbol{P} = \boldsymbol{M}_{\mathbf{1}}(h_1)\boldsymbol{R}\boldsymbol{M}_{\mathbf{2}}(-h_1) \tag{3.101}$$

and h_1 is the layer thickness.

It is considered an infinitesimally thick distribution of normal and tangential springs on the top of the first layer, representing the thin adhesive layer. In that sense, the Eqs. (3.89) and (3.90) are used to compute:

$$\boldsymbol{G}^{+} = (\boldsymbol{I} - i\omega\boldsymbol{G}\boldsymbol{K}^{-1})^{-1}\boldsymbol{G} \tag{3.102}$$

where $\boldsymbol{I}$ is the identity matrix and $\boldsymbol{K}$ is the spring matrix associated to the interfacial adhesive layer. $\boldsymbol{G}^{+}$ is the surface impedance presented to the second elastic layer.

Eqs. (3.99) – (3.102) can be used recursively to determine the surface impedance presented to the upper fluid half-space. Then, this can be used to compute the reflection at the laminate's top. First, we define the reflection coefficient as:

$$r = \frac{\bar{w}_1}{\bar{w}_2} \tag{3.103}$$

where $\bar{w}_2$ is the z (normal) component of the incident displacement field, while $\bar{w}_1$ is the normal component of the reflected displacement field. Since there are only P-waves propagating in the fluid half-space, the other in-plane component of the displacement field can be computed from the normal one, if desired. The classic boundary conditions at the solid/fluid interface are:

$$\boldsymbol{t}^{-} = \boldsymbol{t}^{+} = -\bar{p}\boldsymbol{n} \tag{3.104}$$

$$\bar{w}^{+} = \bar{w}^{-} \tag{3.105}$$

where $\bar{p}$ is the pressure in the fluid that can be computed as $\bar{p} = -i\omega Z_f(\bar{w}_2^{+} - \bar{w}_1^{+})$ and

$\boldsymbol{n}$ is the outward unit vector in the z direction. From the equations above, the following relation can be written:

$$[\boldsymbol{G} + \boldsymbol{Z_f}]\bar{\boldsymbol{u}}^- = \begin{bmatrix} 0 & 0 & 2Z_f\bar{w}_2^+ \end{bmatrix}^T \tag{3.106}$$

Recall that $\boldsymbol{Z_f}$ and Z_f were previously defined in the beginning of this section. r can then be straightforwardly computed as $r = \bar{w}^- - 1$ by solving (3.106) with $\bar{w}_2^+ = 1$.

3.5.1 Methodology of the algorithm

The algorithm that reproduces the computacional procedure was done entirely and manually on MatLab platform, where the frequency and the properties of the laminate are inputs and the reflection coefficient curve is the output, as follows in Figure 3.12.

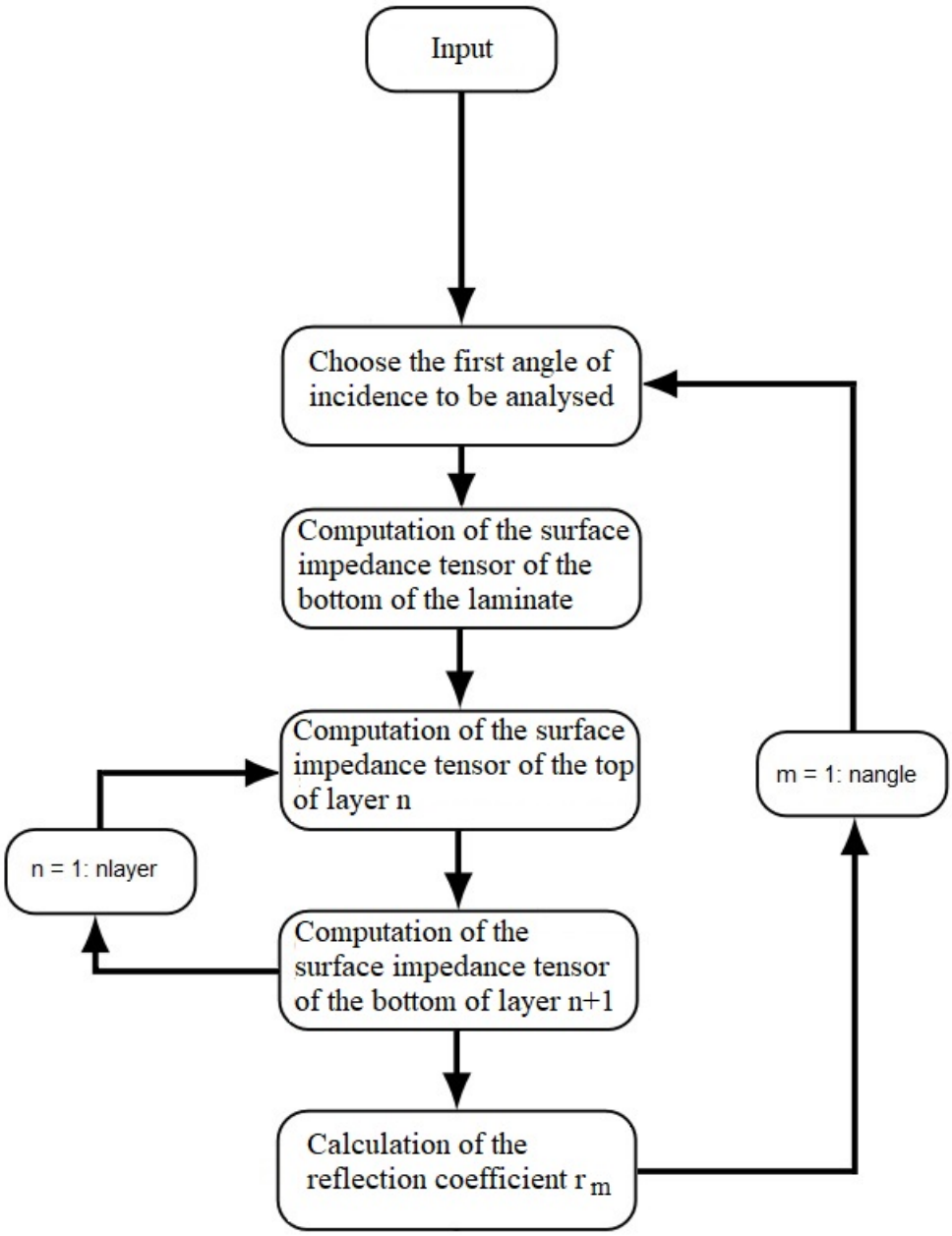

Figure 3.12: Flowchart of the algorithm used to reproduce the computational procedure.

Chapter 4

Results and Discussion

The procedure that is proposed in this Dissertation can be used to obtain the optimum experimental design to be used for defect assessments using ultrasonic inspection. The basic idea consists of determining the angle of incidence and the frequency of the incident wave that provide the outputs that are the most sensitive to flaws at the interfaces.

The incident field is a gaussian beam composed by the superposition of P waves,

Three distinct cases are covered in this chapter. Each of them is represented by a different laminate, which has dimensions considered infinite in the directions xx and yy. This is a reasonable assumption, since we are working with maximum wavelengths in the unit of millimeters. In addition, the stiffness of the adhesive interfaces is homogenized, as well as the defects present in those interfaces.

4.1 Isotropic Laminated Plate Immersed in Acoustic Fluid

The application of the proposed methodology was illustrated by computing the reflection coefficient of a laminate made of a stainless steel layer with 2 cm thickness, an aluminium layer with 3 cm thickness, and a copper layer with 10 cm thickness (in a bottom up fashion). In addition, there is an epoxy layer with 100 μm nominal thickness between each pair of constituent layers, acting as adhesive. The laminate configuration is shown in Figure 4.1 and the wave speeds and density for each constituent layer are given in Table 4.1, as well as for the epoxy.

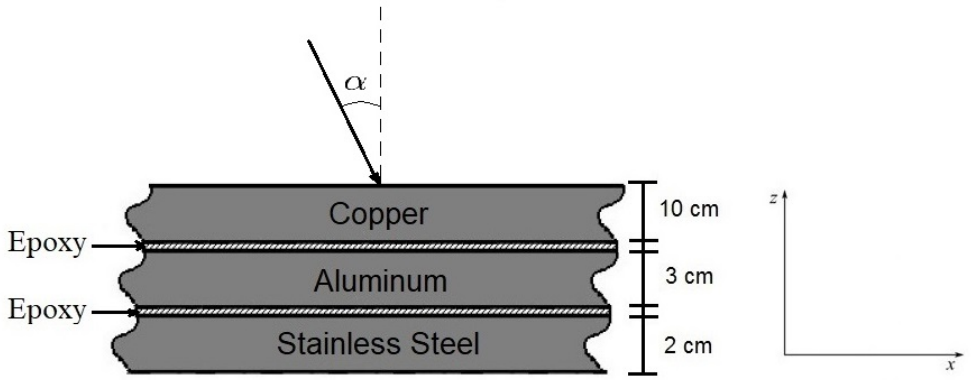

Figure 4.1: The configuration of the three-layer isotropic laminate and the representation of the angle of incidence α.

Table 4.1: Mechanical properties of constituent materials

Material	Density (kg/m^3)	P-wave speed (m/s)	S-wave speed (m/s)
Aluminium	2700	6320	3130
Copper	8930	4660	2160
Epoxy	1200	2150	1030
Stainless Steel	7750	5564	3120
Water	1000	1480	0

Figure 4.2 shows the reflection coefficient r as function of the angle of incidence α for 102.8 kHz. The continuous blue line is related to the flawless laminated plate, the dashed red line is related to a reduced interfacial stiffness component of the interface between the stainless steel and aluminum layers, and the red continuous line represents the incident field spectrum. The interfacial stiffness's xx and yy components were reduced in order to model a kissing bond. The figure 4.2 shows that $\alpha = 4.1^o$ would be a good choice for the angle of incidence.

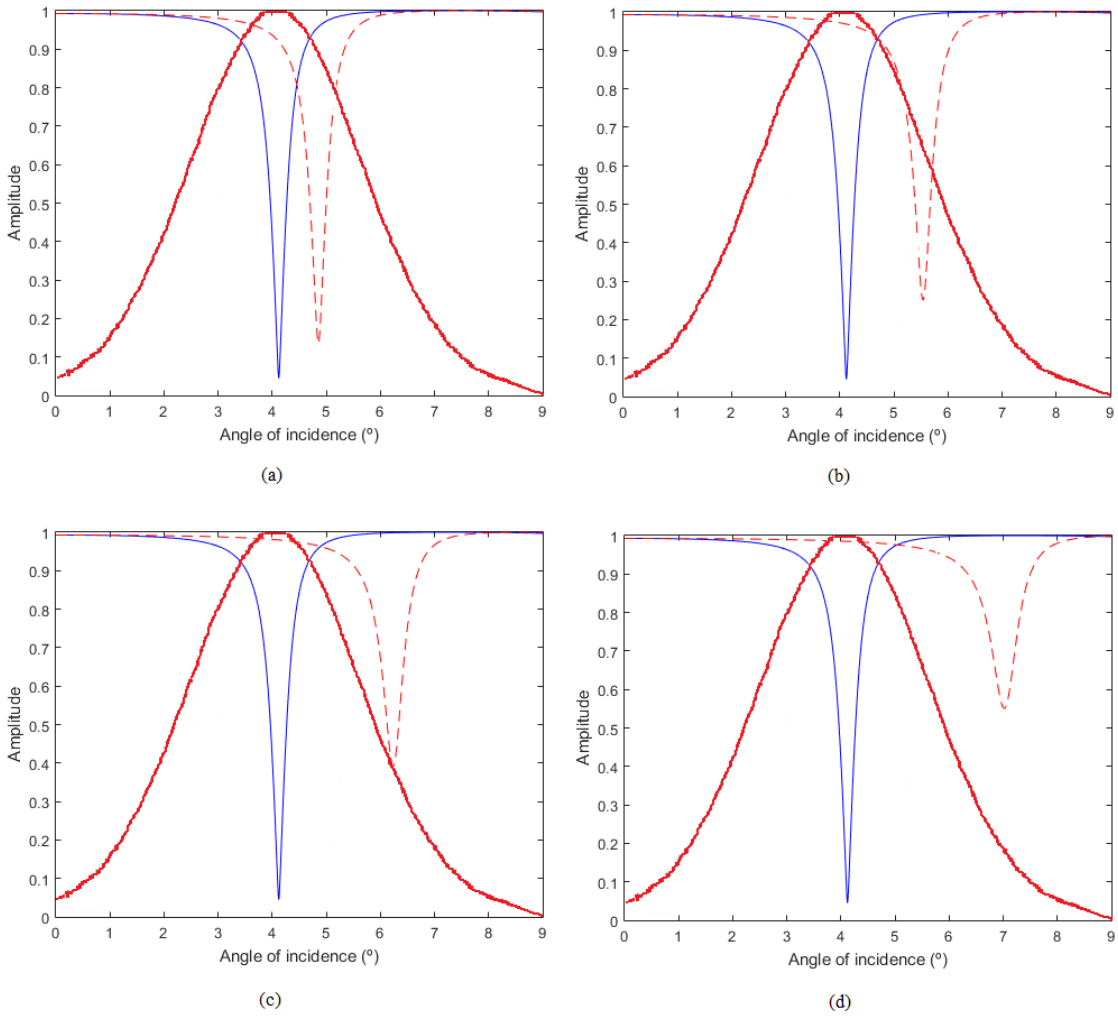

Figure 4.2: Reflection coefficient as function of the angle of incidence. The defect is in the first adhesive layer, in the transversal direction. (a) 80% of original stiffness. (b) 60% of original stiffness. (c) 40% of original stiffness. (d) 20% of original stiffness.

For a better illustration of the problem, the reflected field corresponding to the incident field is shown in Figure 4.3. To generate this field, each point of the incident spectrum is multiplied by the corresponding reflection coefficient. After that, an inverse Fourier transform in the spatial domain is performed in x, obtaining the reflected field at the top of the laminate. Note that the maximum amplitude of the spectrum is related to the minimum of the reflection coefficient curve, this is desirable in order to obtain a greater sensitivity in the field reflected in relation to the defect in the interface.

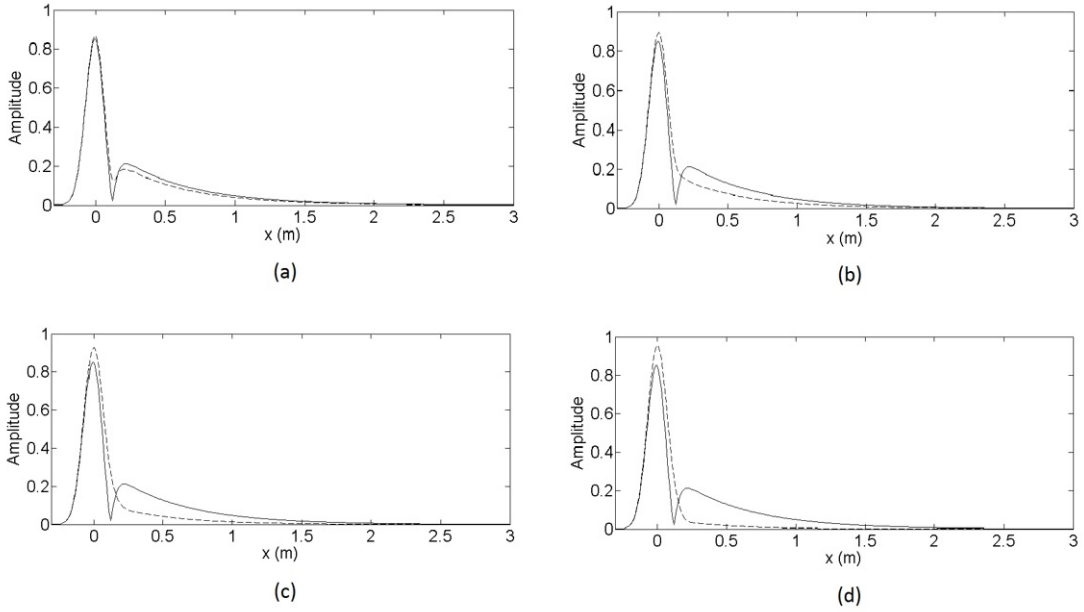

Figure 4.3: Reflected field for defect in the first adhesive layer, in the transversal direction. The continuous line represents the reflection field in a perfect adhesive layer and the dashed line is the reflection field in a flawed adhesive layer. (a) 80% of original stiffness. (b) 60% of original stiffness. (c) 40% of original stiffness. (d) 20% of original stiffness.

This reflected field has two "hills". One of them, of greater amplitude, around $x = 0$, corresponds to the specular reflection and the lateral lobe, around $x = 0.25m$, corresponds to a leak pattern, in which there is leakage of energy. Note that the leak pattern starts to disappear as the defect intensifies at the interface, if it is possible to measure this region with a transducer, it would be possible to easily identify if there are defects in the analyzed region.

Figure 4.4 shows the reflection coefficient r as function of the angle of incidence for α 128.4 kHz. The continuous blue line is again related to the flawless laminated plate, the dashed red line is related to a reduced interfacial stiffness component of the interface between the stainless steel and aluminum layers, and the red continuous line represents the incident field spectrum. The interfacial stiffness's zz component was reduced. The Figure 4.4 shows that a normal incidence or $\alpha = 0^o$ would be a good choice for the angle of incidence.

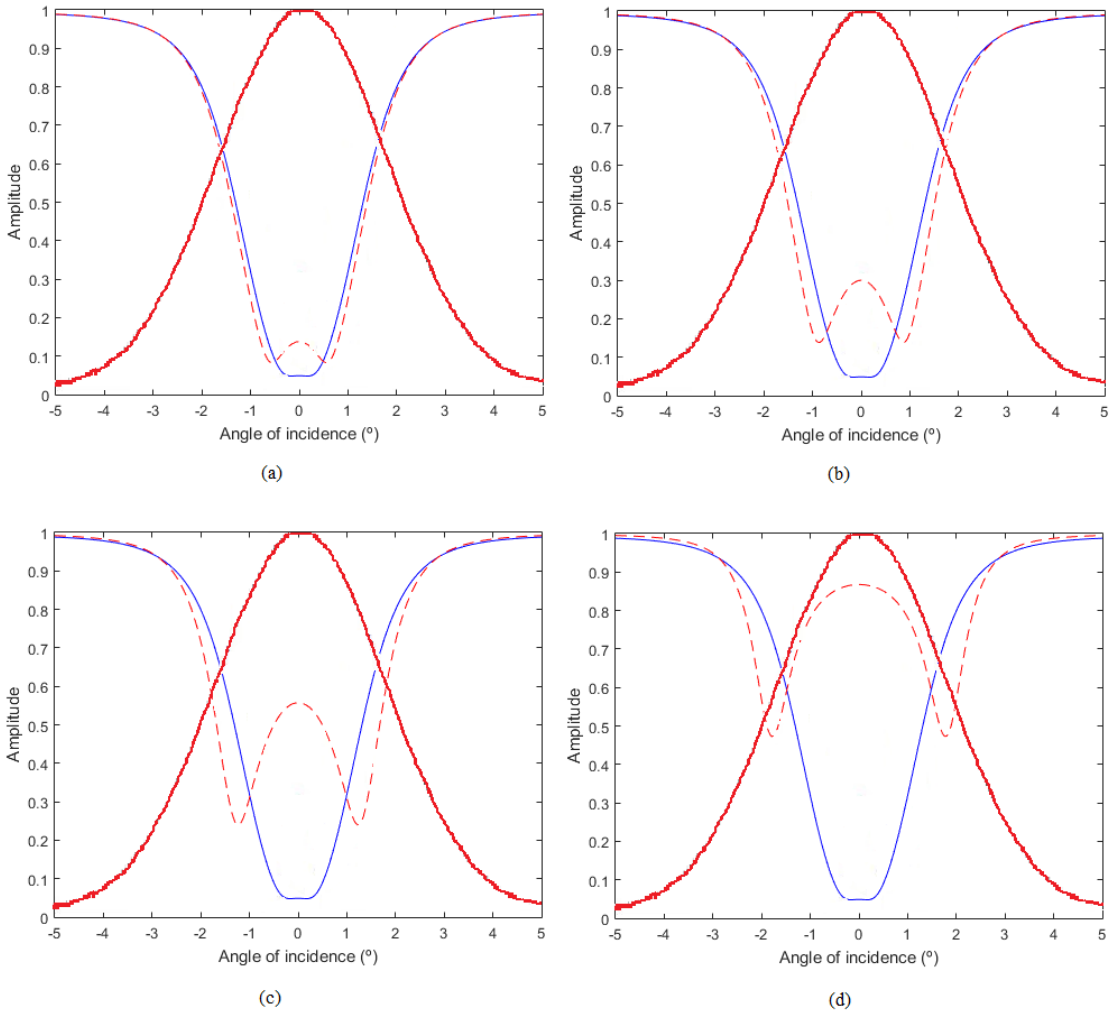

Figure 4.4: Reflection coefficient as function of the angle of incidence. The defect is in the first adhesive layer, in the normal direction. (a) 80% of original stiffness. (b) 60% of original stiffness. (c) 40% of original stiffness. (d) 20% of original stiffness.

Once again, the reflected field corresponding to the incident field is shown in Figure 4.5. The method used to generate this field is the same as that shown earlier in this section.

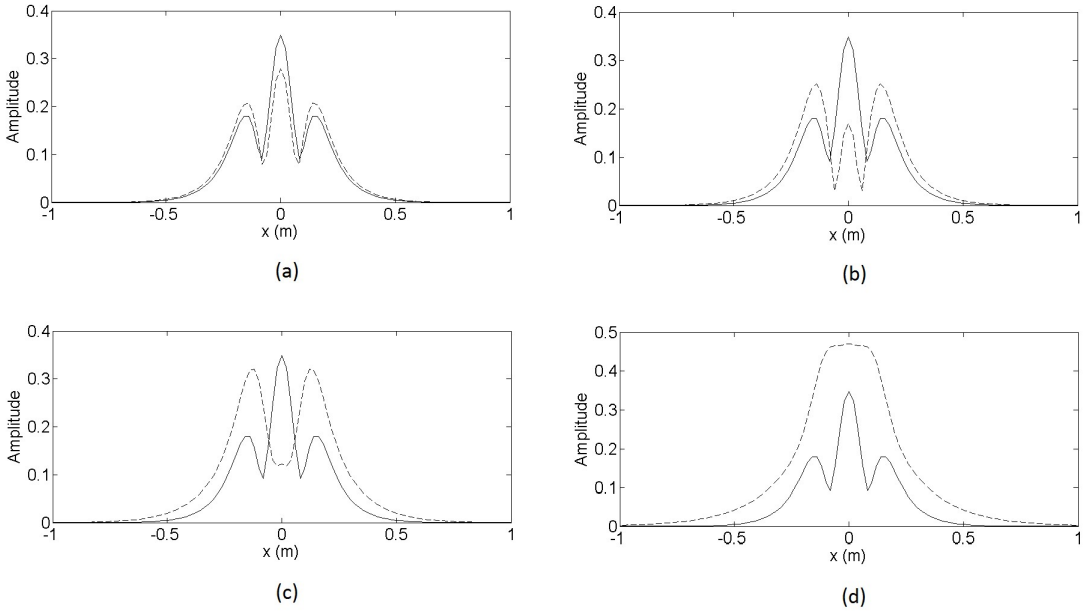

Figure 4.5: Reflected field for defect in the first adhesive layer, in the normal direction. The continuous line represents the reflection field in a perfect adhesive layer and the dashed line is the reflection field in a flawed adhesive layer. (a) 80% of original stiffness. (b) 60% of original stiffness. (c) 40% of original stiffness. (d) 20% of original stiffness.

This reflected field has three "hills". The middle one, of greater amplitude, around $x = 0$, corresponds to the specular reflection and the lateral lobes, around $x = 0.25m$ and $x = -0.25m$, correspond to leak patterns. The leak patterns start to disappear as the defect intensifies at the interface, generating only one "hill" of greater amplitude, making it possible to measure the region with a transducer.

Figure 4.6 shows the reflection coefficient r as function of the angle of incidence α for 96.5 kHz. The continuous blue line is one more time related to the flawless laminated plate, while the dashed red line is related to a reduced interfacial stiffness component of the interface between the aluminum and copper layers. The interfacial stiffness's xx and yy components were reduced in order to model a kissing bond. The figure 4.6 shows that $\alpha = 9.2^o$ would be a good choice for the angle of incidence.

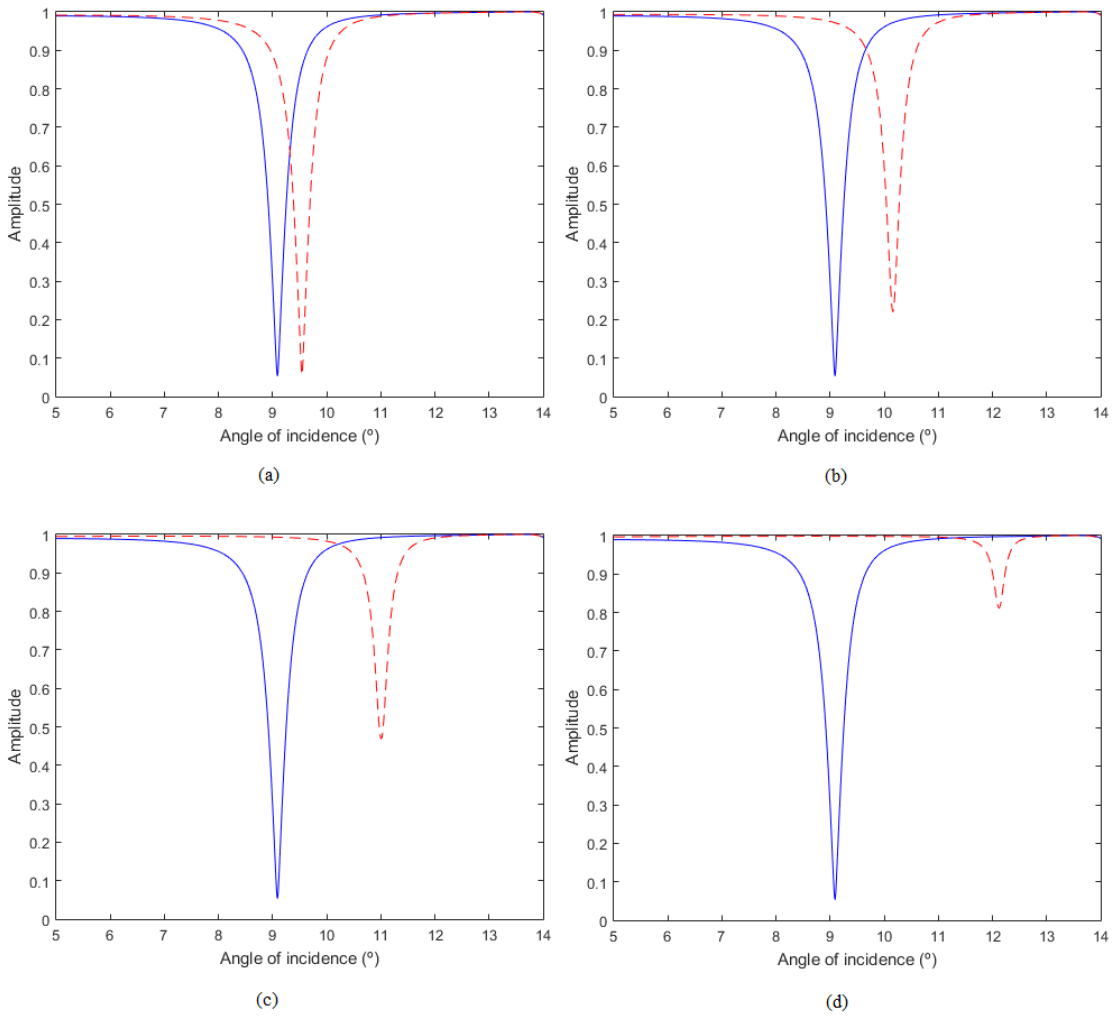

Figure 4.6: Reflection coefficient as function of the angle of incidence. The defect is in the second adhesive layer, in the transversal direction. (a) 80% of original stiffness. (b) 60% of original stiffness. (c) 40% of original stiffness. (d) 20% of original stiffness.

Figure 4.7 shows the reflection coefficient r as function of the angle of incidence α for 102.8 kHz. The continuous blue line is, for the last time, related to the flawless laminated plate, while the dashed red line is related to a reduced interfacial stiffness component of the interface between the aluminum and copper layers. The interfacial stiffness's zz component was reduced. The figure 4.7 shows again that a normal incidence or $\alpha = 0^o$ would be a good choice for the angle of incidence.

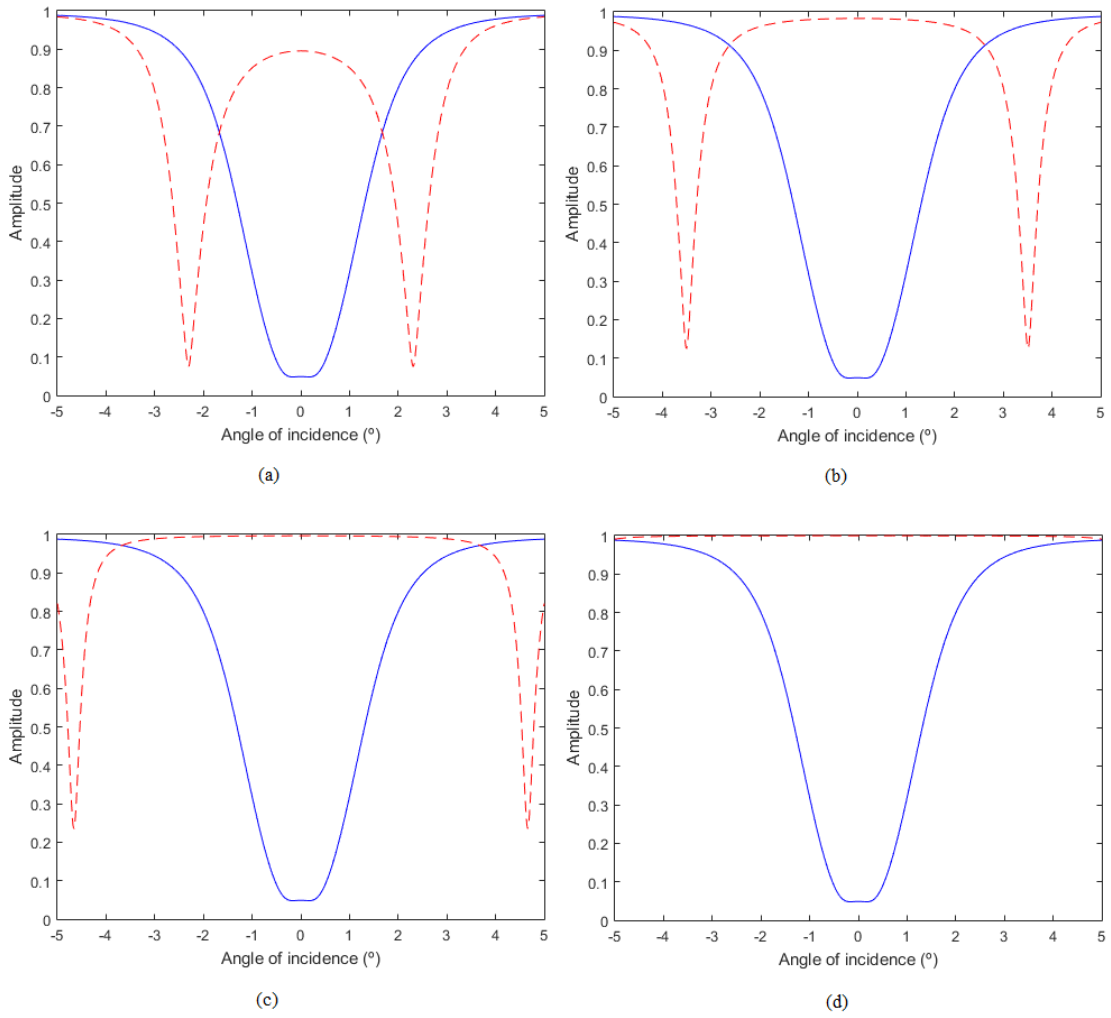

Figure 4.7: Reflection coefficient as function of the angle of incidence. The defect is in the second adhesive layer, in the normal direction. (a) 80% of original stiffness. (b) 60% of original stiffness. (c) 40% of original stiffness. (d) 20% of original stiffness.

4.2 Anisotropic Laminated Plate Immersed in Acoustic Fluid

In order to explore a more complex example, the response of a 16-ply, symmetric, quasi-isotropic, composite laminate with a $[0^o/45^o/-45^o/90^o]_{2S}$ stacking sequence is analysed. The graphite-epoxy, unidirectional, fiber reinforced layers have equal thicknesses of 0.19 mm. The layers, with mass density of 1.6 g/cm^3, are considered transversely isotropic and the plate configuration can be seen in the Figure 4.8. The non-zero elastic constants, in Voigt notation, are listed in Table 4.2, where the subscript 3 corresponds to the direction of the reinforcing fibers. This means, for instance, that directions 3 and x are the same for the layers oriented at 0^o. For each layer, the elastic constants were rotated around the material 1-axis using standard methods [49].

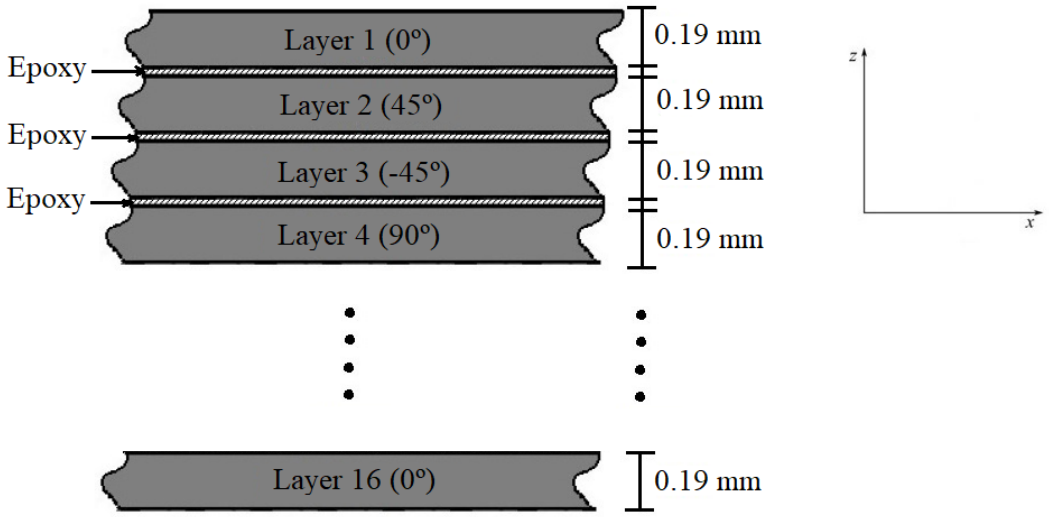

Figure 4.8: The configuration of the sixteen-layer anisotropic laminate.

Table 4.2: Non-zero elastic constants of the transversely isotropic, graphite-epoxy fiber reinforced layers [50]. Values are listed in GPa. Voigt notation is employed and the material 3-axis corresponds to the fiber reinforcement direction.

C_{11}	C_{12}	C_{13}	C_{22}	C_{23}	C_{33}	C_{44}	C_{55}	C_{66}
14.5	7.24	6.5	14.5	6.5	161	7.1	7.1	3.63

There is a thin interfacial adhesive epoxy layer with 4 μm nominal thickness between each fiber reinforced ply. The wave speed and density considered for the epoxy are shown in Table 4.1. In the context of the QSA, when intact, this thin epoxy layer can be modeled by an equivalent interfacial stiffness, similarly to the three-layer isotropic plate analysed in the previous subsection.

Figure 4.9 shows the reflection coefficient r as function of the angle of incidence α for 4.3 MHz. The continuous blue line is related to the flawless laminated plate, while the dashed red line is related to a reduced interfacial stiffness component of the interface between the eighth and ninth anisotropic layers. The interfacial stiffness's xx and yy components were reduced in order to model a kissing bond. The figure 4.9 shows that $\alpha = 15.9^o$ would be a good choice for the angle of incidence.

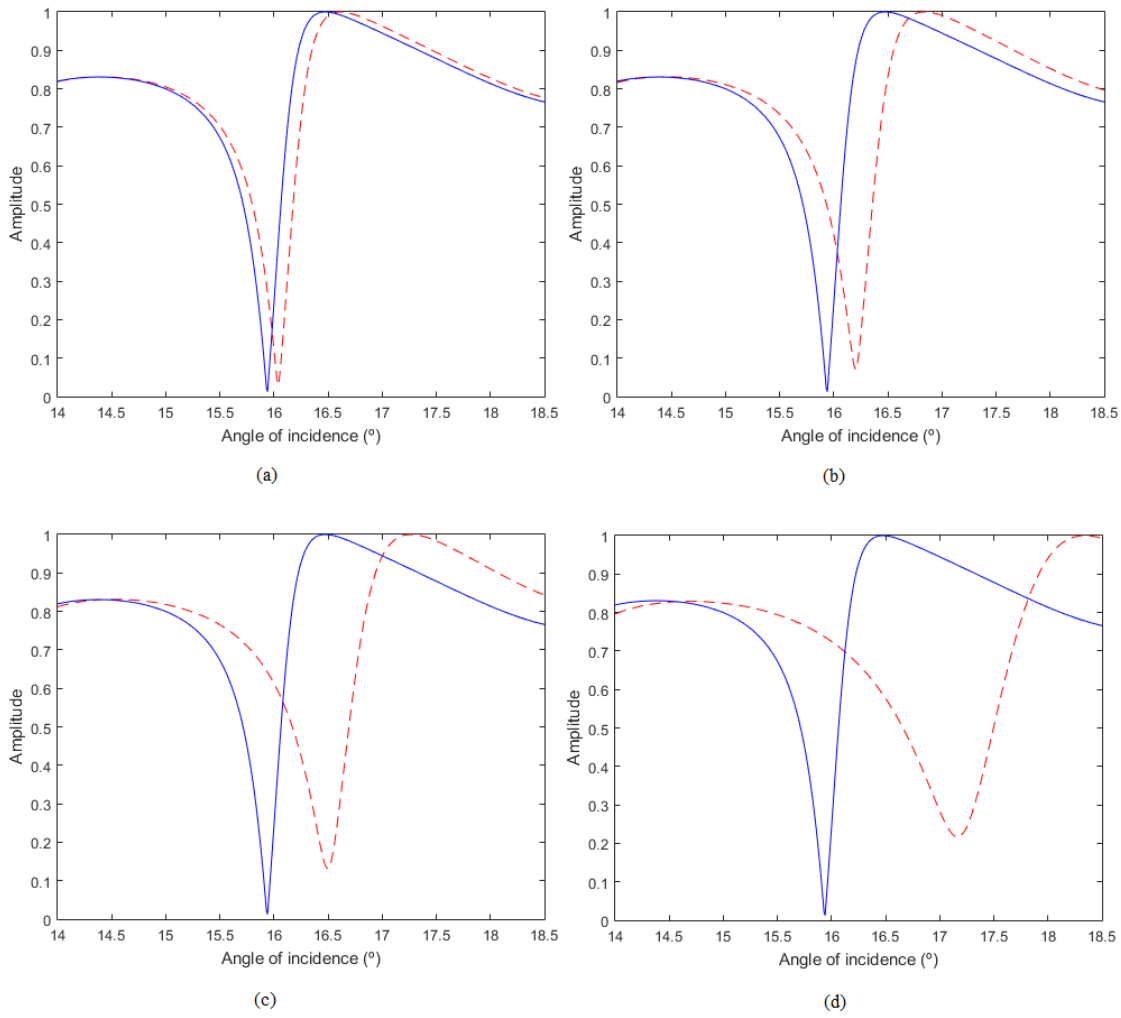

Figure 4.9: Reflection coefficient as function of the angle of incidence. The defect is in the eighth adhesive layer, in the transversal direction. (a) 80% of original stiffness. (b) 60% of original stiffness. (c) 40% of original stiffness. (d) 20% of original stiffness.

Figure 4.10 shows the reflection coefficient r as function of the angle of incidence α for 4.8 MHz. The continuous blue line is again related to the flawless laminated plate, while the dashed red line is related to a reduced interfacial stiffness component of the interface between the eighth and ninth anisotropic layers. The interfacial stiffness's zz component was reduced. The figure 4.10 shows that a normal incidence or $\alpha = 0^o$ would be a good choice for the angle of incidence.

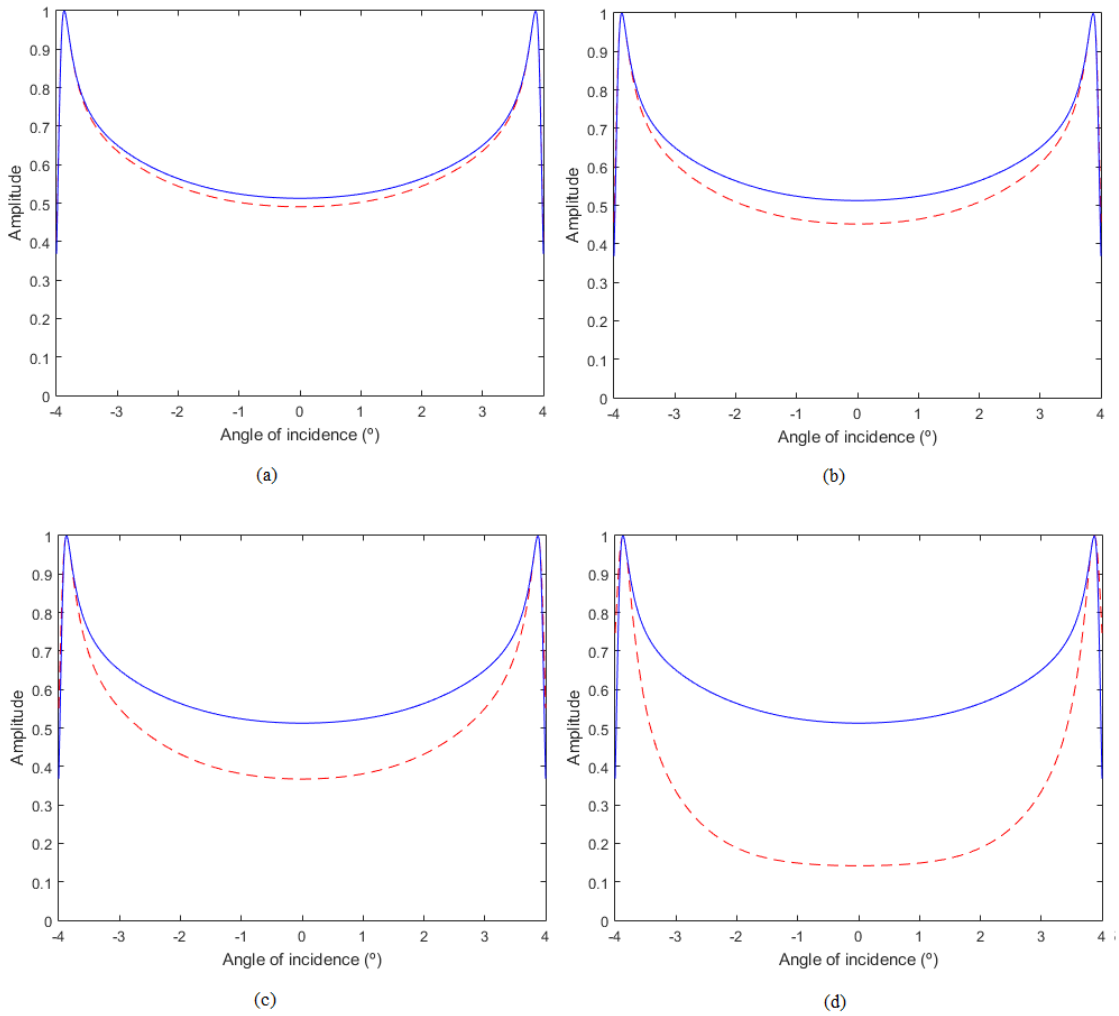

Figure 4.10: Reflection coefficient as function of the angle of incidence. The defect is in the eighth adhesive layer, in the transversal direction. (a) 80% of original stiffness. (b) 60% of original stiffness. (c) 40% of original stiffness. (d) 20% of original stiffness.

Figure 4.11 shows the reflection coefficient r as function of the angle of incidence α for 5.2 MHz. The continuous blue line is one more time related to the flawless laminated plate, the dashed red line is related to a reduced interfacial stiffness component of the interface between the eighth and ninth layers, and the red continuous line represents the incident field spectrum. The interfacial stiffness's xx and yy components were reduced in order to model a kissing bond. The figure 4.11 shows that $\alpha = 5.6^o$ would be a good choice for the angle of incidence.

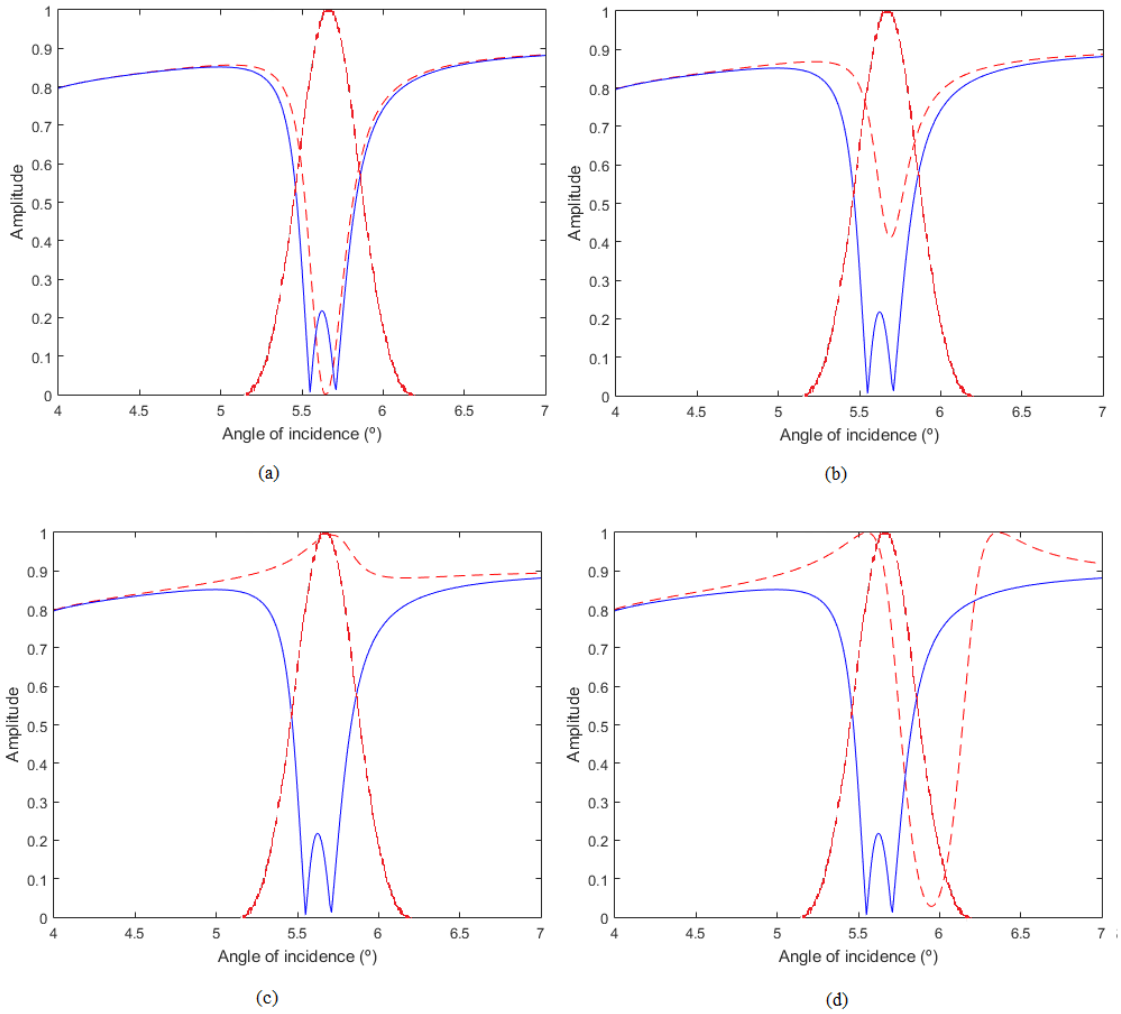

Figure 4.11: Reflection coefficient as function of the angle of incidence. The defect is in the ninth adhesive layer, in the transversal direction. (a) 80% of original stiffness. (b) 60% of original stiffness. (c) 40% of original stiffness. (d) 20% of original stiffness.

The reflected field corresponding to the incident field is shown in Figure 4.12. The method used to generate this field is the same as that shown in the isotropic plate case.

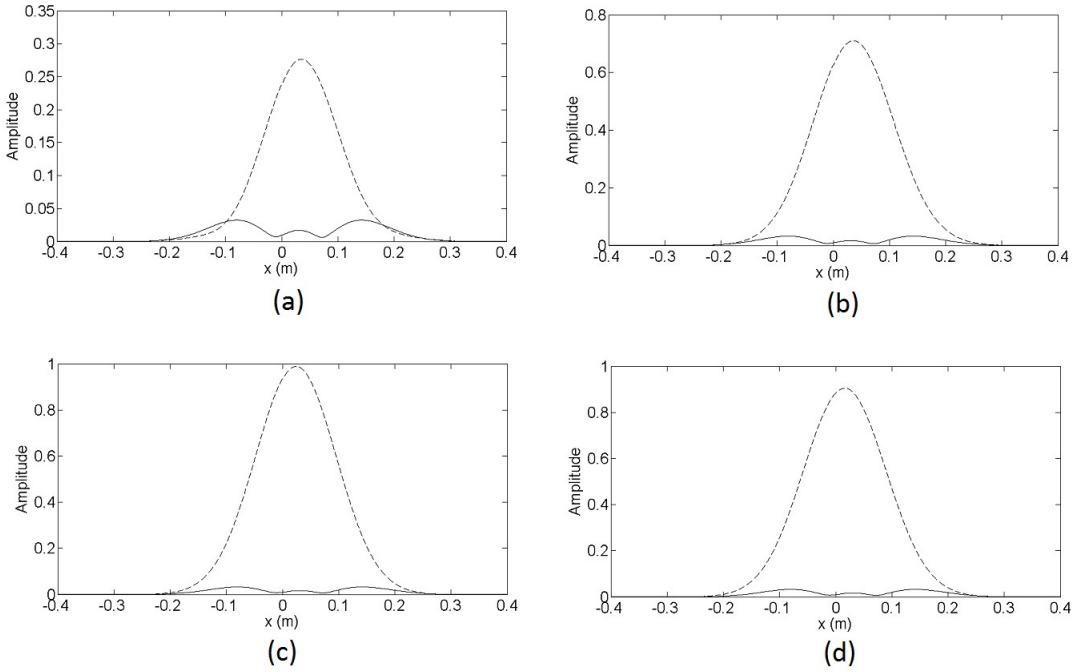

Figure 4.12: Reflection coefficient as function of the angle of incidence. The defect is in the first adhesive layer, in the transversal direction. The continuous line represents the reflection field in a perfect adhesive layer and the dashed line is the reflection field in a flawed adhesive layer. (a) 80% of original stiffness. (b) 60% of original stiffness. (c) 40% of original stiffness. (d) 20% of original stiffness.

It is possible to note that, even in a much complex scenario, there are significant changes between the reflected field from the flawless plate and the plate with defect in the ninth interface. That is, it would be easy to identify such defects through the experimental procedure using the obtained parameters of the incident field.

Figure 4.13 shows the reflection coefficient r as function of the angle of incidence α for 5.3 MHz. The continuous blue line is, for the last time, related to the flawless laminated plate, the dashed red line is related to a reduced interfacial stiffness component of the interface between the ninth and tenth anisotropic layers, and the red continuous line represents the incident field spectrum. The interfacial stiffness's zz component was reduced. The figure 4.13 shows again that a normal incidence or $\alpha = 0^]$ would be a good choice for the angle of incidence.

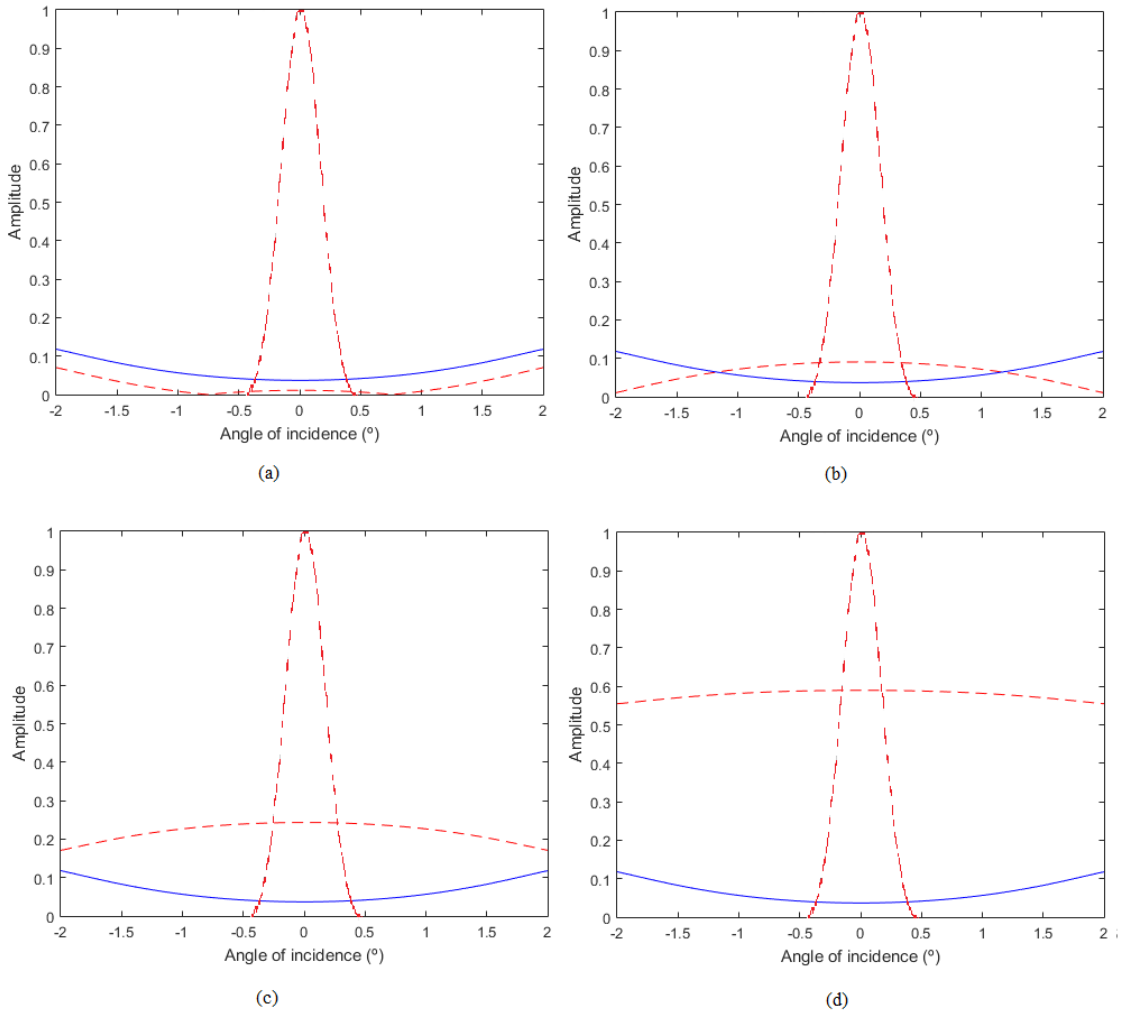

Figure 4.13: Reflection coefficient as function of the angle of incidence. The defect is in the ninth adhesive layer, in the transversal direction. (a) 80% of original stiffness. (b) 60% of original stiffness. (c) 40% of original stiffness. (d) 20% of original stiffness.

One more time, the reflected field corresponding to the incident field is shown in Figure 4.14. The method used to generate this field is the same as before.

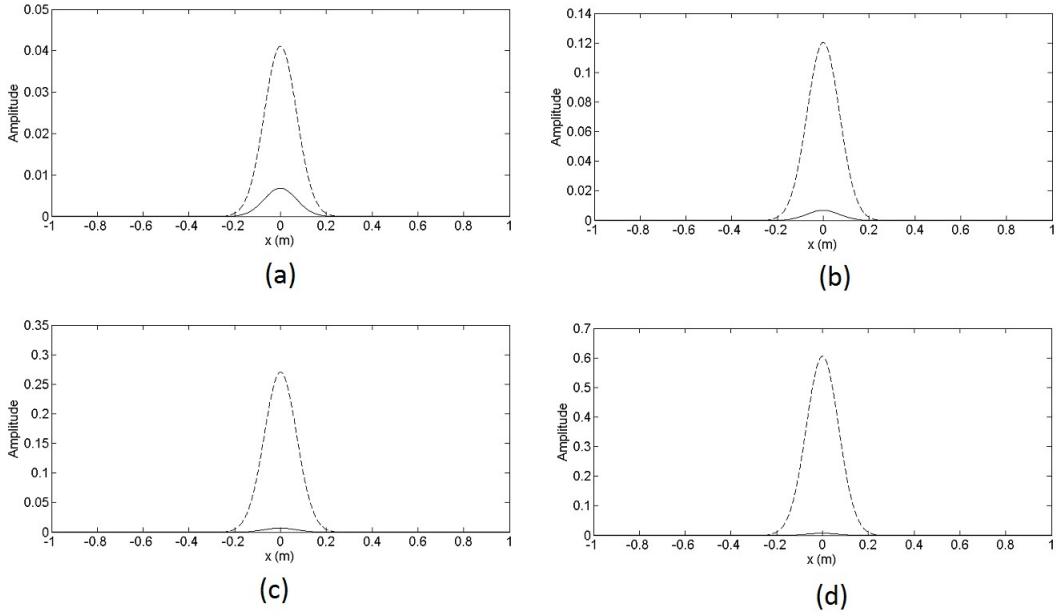

Figure 4.14: Reflection coefficient as function of the angle of incidence. The defect is in the first adhesive layer, in the transversal direction. The continuous line represents the reflection field in a perfect adhesive layer and the dashed line is the reflection field in a flawed adhesive layer. (a) 80% of original stiffness. (b) 60% of original stiffness. (c) 40% of original stiffness. (d) 20% of original stiffness.

For defect in the zz direction, there are, once again, significant changes between the reflected field from the flawless plate and a flawed one. This show how sensible and stable is the computational procedure, no matter the complexity in the mathematical modeling of the problem physics.

4.3 Cemented Rising Tube

The QSA could also be used to model rough contact surfaces, an example of a simple cemented rising tube can be explored for this purpose [1, 9, 34]. With this, it is possible to analyze the feasibility of using the method as an auxiliary tool for the abandonment of cemented oil wells, taking into account a considerable saving in the expense of the entire process.

The experimental procedure uses a tool that moves along the entire inner part of the tube, carrying a transducer, which can excites sonic and ultrasonic waves, and a set of receivers, which measure the attenuation of the waves along the borehole axis direction [1]. The whole tool configuration can be seen in Figure 4.15.

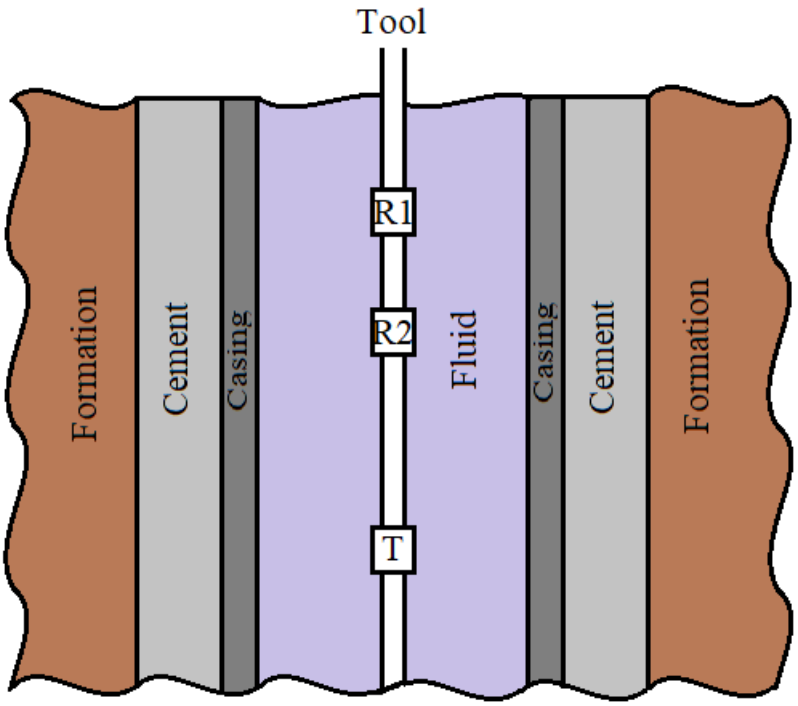

Figure 4.15: The configuration of the experimental tool, where T is the transducer, and R1 and R2 are the two receptors.

The system is composed by an inner fluid, a casing tube, a layer of cement surrounding the tube and the rock formation [1]. Since the wavelength used for inspection is really small compared to the tube curvature, the system can be approximated to a flat plate [1]. The system configuration and the dimensions of the layers are shown in Figure 4.16 and the wave speeds and density for each constituent layer are listed in Table 4.3.

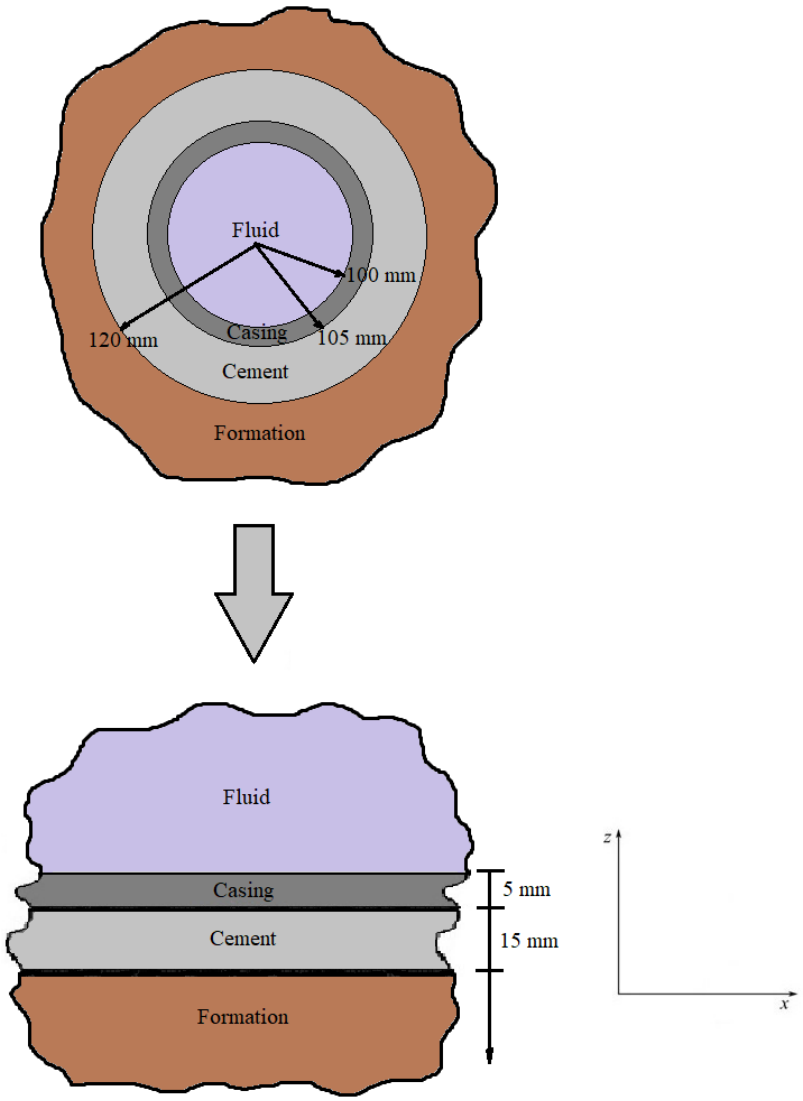

Figure 4.16: Simple cemented rising tube configuration and dimensions, as well as the approximation to a flat system [1].

Table 4.3: Parameters of the relevant materials that constitute the complete system of a cemented rising tube [1].

Material	Density (kg/m^3)	P-wave speed (m/s)	S-wave speed (m/s)
Formation	2320	4500	2455
Casing	7850	5860	3130
Conventional cement	1920	2823	1729

Since there is no information about the bonding interfaces of the system in literature, it was necessary to make an approximation. Each property of the bonding interfaces was approximated by an arithmetic mean of the properties of the anterior and posterior

constituent layers. The thickness of the interface between the casing and the cement is supposed to be 1 μm, and the interface between the cement and the rock formation is 1 mm thick, due to the high roughness of a natural formation. After acquiring the properties of the interfaces, the QSA is used analogously to the previous cases.

It is important to note that the bottom of this laminate has a solid in its boundary and not a fluid, as in the previous cases. This leads to the addition of SV and SH waves propagating in the lower medium to the plate, and the surface impendance tensor of the bottom of the laminate is now equal to the downgoing impendance tensor of the rock formation $\boldsymbol{Z_2}$.

The main problem of this system is to identify defects inside the cement layer, and the interface between the cement and the formation is where the current methods proposed in the literature [1] find more difficulty, so that the analysis focuses on this specific point.

Figure 4.17 shows the reflection coefficient r as function of the angle of incidence α for 330 kHz. The continuous blue line is related to the flawless laminated plate, while the dashed red line is related to a reduced interfacial stiffness component of the interface between the cement and the rock formation. The interfacial stiffness's xx and yy components were reduced. The figure 4.17 shows that $\alpha = 23.3^o$ would be a good choice for the angle of incidence.

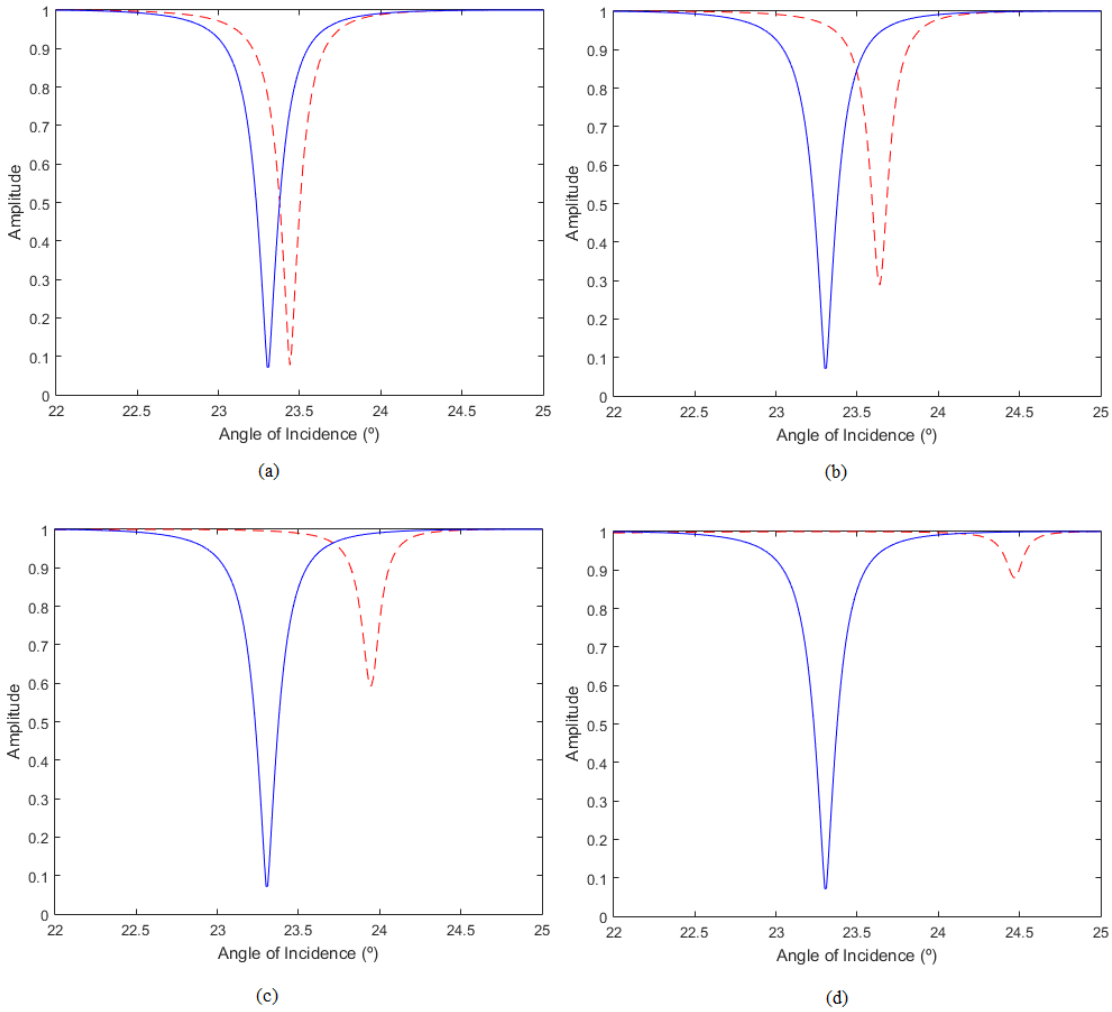

Figure 4.17: Reflection coefficient as function of the angle of incidence. The defect is in the first adhesive layer, in the transversal direction. (a) 80% of original stiffness. (b) 60% of original stiffness. (c) 40% of original stiffness. (d) 20% of original stiffness.

Figure 4.18 shows the reflection coefficient r as function of the angle of incidence α for 262 kHz. The continuous blue line is again related to the flawless laminated plate, while the dashed red line is related to a reduced interfacial stiffness component of the interface between the cement and the rock formation. The interfacial stiffness's zz component was reduced. The figure 4.18 shows that $\alpha = 36.5^o$ would be a good choice for the angle of incidence.

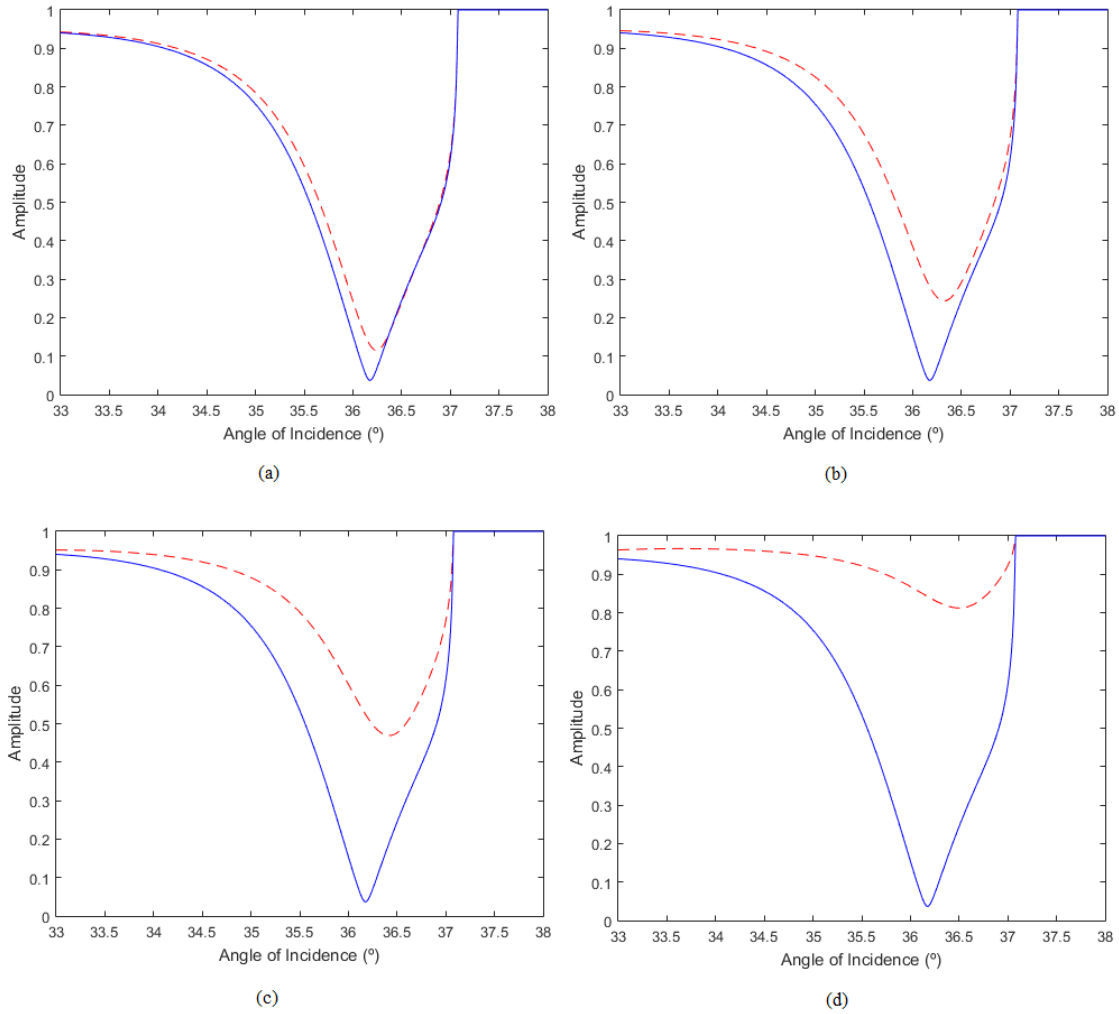

Figure 4.18: Reflection coefficient as function of the angle of incidence. The defect is in the first adhesive layer, in the transversal direction. (a) 80% of original stiffness. (b) 60% of original stiffness. (c) 40% of original stiffness. (d) 20% of original stiffness.

The obtained result in the direction zz is very interesting and plausible in comparison with the information acquired in the literature, since its similar to the pairs of frequency and angle of incidence chosen in [9, 51].

It is important to mention that tests were carried out also placing defect in the interface between the casing and the cement, besides the defect already present in the analyzed interface. With this, it was possible to verify that even for simultaneous defects in the two interfaces, the obtained field is only sensible to flaws in the analysed interface, making it even more reliable for analysis in only one specific interface, as it does not have deviations caused by other defects present in the laminate.

Furthermore, it is worth mentioning that the angle of incidence doesn't have to be exactly the optimal angle obtained in order to analyse a defect, since it's nearly impossible to calibrate the experimental tools to achieve exactly that angle. There is a range of angles around the optimal one that are still great candidates to carry out the measurements. With that in mind, we can proceed to the conclusions.

Chapter 5

Conclusions

The present work was concluded in seven stages, as follows:

- A systematic modelling procedure to identify the harmonic ultrasonic incident inspecting fields, that most strongly interact with bonding defects, is proposed.
- The constituent layers are modeled with the classical wave theory in elastic solids.
- The bonding interfaces are modeled with the aid of the spring boundary conditions, applying the Quasi-Static Approximation.
- The invariant embedding technique is used to compute the reflection coefficient at the top of the immersed laminates. The main advantage of this technique is its unconditional numerical stability even for evanescent waves at high frequencies. Besides, it is computationally very efficient and easy to implement. The developed algorithm is equally well suited to treating isotropic as well as anisotropic layers.
- The results for a three-layer isotropic plate immersed in water are generated and analysed.
- The results for a 16-ply anisotropic composite laminate used in the aeronautical industry, immersed in water, are generated and analysed.
- The results for a simple cemented rising tube system are generated and analysed.

The optimal parameters used in a ultrasonic inspection in order to identify defects in the transverse direction of the adhesive bonds were successfully obtained by analysing the reflection coefficient r in both isotropic and anisotropic cases. In this type of defects, called kissing bonds, these parameters are generally more difficult to obtain. In addition, the optimal choice for the angle of incidence varies for each case. Furthermore, the flaws in the normal direction can be all identified with an angle of incidence of 0^{o}. This is an interesting result, since it is the easiest angle to position the transmitters in the experimental procedure. It is still possible to note that even though the anisotropic model has a higher degree of complexity, the method still worked perfectly, but the optimal frequencies had an increase of one order of magnitude for the method to maintain its sensitivity.

Another interesting result came from the cemented rising tube system, where the cement-formation interface was analysed. In the transversal direction, the optimal parameters were obtained in an analogous way to the case of the three-layer isotropic

plate. In the normal direction also, but the optimal pairs of angle of incidence and frequency were very close to those cited in the literature, in which the angles vary from 33° to 38° and the frequency range is around 250 kHz [1, 9, 34, 51]. It is important to note that these works use a different method to identify interfaces flaws.

The results enhance the potential of ultrasound to reveal bonding defects. For all the simulations, it was possible to determine frequencies and angles of incidence for which the reflection coefficient changes significantly in response to interfacial stiffness reduction, leading to the belief that these changes would be measurable in actual ultrasonic inspections. In that sense, it is expected that the proposed methodology may serve to aid in the design of ultrasound interface inspection and characterization methods.

For future works, a cemented rising tube system of a higher degree of complexibility can be analysed, such as a double casing, with fluid between the two tubes. This is a well known problem in literature and to find a reliable way to identify defects on the outermost interface is still an open task. Another proposal is to consider the curvature of the system and compare to the flat plate approach.

Besides that, the chosen angle of incidence and frequency to identify the defects in the bonding interfaces are also the optimal choices for the inspecting field in inverse problems for interfacial stiffness estimation, this can be explored and lead to a new range of works in this area.

Bibliography

[1] WANG, H., TAO, G., SHANG, X. "Understanding acoustic methods for cement bond logging", *The Journal of the Acoustical Society of America*, v. 139, n. 5, pp. 2407–2416, 2016. doi: 10.1121/1.4947511. Disponível em: <https://doi.org/10.1121/1.4947511>.

[2] KACZMAR, J., PIETRZAK, K., WŁOSIŃSKI, W. "The production and application of metal matrix composite materials", *Journal of Materials Processing Technology*, v. 106, n. 1, pp. 58 – 67, 2000. ISSN: 0924-0136. doi: https://doi.org/10.1016/S0924-0136(00)00639-7. Disponível em: <http://www.sciencedirect.com/science/article/pii/S0924013600006397>.

[3] JONES, R. M. *Mechanics of composite materials*, v. 193. Scripta Book Company Washington, DC, 1975.

[4] ROKHLIN, S. I., LAVRENTYEV, A. I., LI, B. "Ultrasonic evaluation of environmental durability of adhesive joints", *Research in Nondestructive Evaluation*, v. 5, n. 2, pp. 95–109, Mar 1993. ISSN: 1432-2110. doi: 10.1007/BF01606359. Disponível em: <https://doi.org/10.1007/BF01606359>.

[5] LAVRENTYEV, A. I., ROKHLIN, S. I. "Models for ultrasonic characterization of environmental degradation of interfaces in adhesive joints", *Journal of Applied Physics*, v. 76, n. 8, pp. 4643–4650, 1994. doi: 10.1063/1.357301. Disponível em: <https://doi.org/10.1063/1.357301>.

[6] SMITH, R. "Composite defects and their detection", *Materials science and engineering*, v. 3, pp. 103–143, 2009.

[7] BLYTH, M., HUPP, D., WHYTE, I., et al. "LWD Sonic Cement Logging: Benefits Applicability And Novel Uses For Assessing Well Integrity", 03 2013.

[8] KIRAN, R., TEODORIU, C., DADMOHAMMADI, Y., et al. "Identification and evaluation of well integrity and causes of failure of well integrity barriers (A review)", *Journal of Natural Gas Science and Engineering*, v. 45, n. Supplement C, pp. 511 – 526, 2017. ISSN: 1875-5100. doi: https://doi.org/10.1016/j.jngse.2017.05.009. Disponível em: <http://www.sciencedirect.com/science/article/pii/S1875510017302184>.

[9] VIGGEN, E. M., JOHANSEN, T. F., MERCIU, I.-A. "Simulation and modeling of ultrasonic pitch-catch through-tubing logging", *GEOPHYSICS*, v. 81, n. 4, pp. D383–D393, 2016. doi: 10.1190/geo2015-0251.1. Disponível em: <https://doi.org/10.1190/geo2015-0251.1>.

[10] PIALUCHA, T., CAWLEY, P. "The detection of a weak adhesive/adherend interface in bonded joints by ultrasonic reflection measurements", *Rev. Prog. Quant. Nondestr. Eval.*, v. 11, pp. 1261–1266, 1992.

[11] LI, B., HEFETZ, M., ROKHLIN, S. I. "Ultrasonic evaluation of environmentally degraded adhesive joints", *Rev. Prog. Quant. Nondestr. Eval.*, v. 11, pp. 1221–1228, 1992.

[12] PILARSKI, A., ROSE, J. L., BALASUBRAMANIAM, K. "The angular and frequency characteristics of reflectivity from a solid layer embedded between two solids with imperfect boundary conditions", *J. Acoust. Soc. Am.*, v. 87, pp. 532–542, 1990.

[13] BALTAZAR, A., ROKHLIN, S. I., PECORARI, C. "On the relationship between ultrasonic and micro-structural properties of imperfect interfaces in layered solids", *Rev. Prog. Quant. Nondestr.*, v. 18, pp. 1463–1470, 1999.

[14] CASTAINGS, M., SIRYABE, E., RENIER, M., et al. "Ultrasonic characterization of cohesive and adhesive properties of adhesive bonds", v. 138, pp. 1766–1766, 09 2015.

[15] MOYSAN, J., GALY, J., SIRYABE, E., et al. "Innovating for Structural Adhesive Bonding Evaluation and Analysis with Ultrasounds : A Summary", 06 2016.

[16] MAL, A. "Guided waves in layered solids with interface zones", *International Journal of Engineering Science*, v. 26, n. 8, pp. 873 – 881, 1988. ISSN: 0020-7225. doi: https://doi.org/10.1016/0020-7225(88)90038-9. Disponível em: <http://www.sciencedirect.com/science/article/pii/0020722588900389>.

[17] HELLER, K., JACOBS, L., QU, J. "Characterization of adhesive bond properties using Lamb waves", *NDT E International*, v. 33, n. 8, pp. 555 – 563, 2000. ISSN: 0963-8695. doi: https://doi.org/10.1016/S0963-8695(00)00022-0. Disponível em: <http://www.sciencedirect.com/science/article/pii/S0963869500000220>.

[18] TELLER, C. M., DIERCKS, K. J., BAR-COHEN, Y., et al. "Nondestructive Evaluation of Adhesive Bonds Using Leaky Lamb Waves". In: Thompson, D. O., Chimenti, D. E. (Eds.), *Review of Progress in Quantitative Nondestructive Evaluation: Volume 7B*, pp. 935–942, Boston, MA, Springer US, 1988. ISBN: 978-1-4613-0979-6. doi: 10.1007/978-1-4613-0979-6_7. Disponível em: <https://doi.org/10.1007/978-1-4613-0979-6_7>.

[19] LOWE, M. J. S., CAWLEY, P. "The applicability of plate wave techniques for the inspection of adhesive and diffusion bonded joints", *Journal of Nondestructive Evaluation*, v. 13, n. 4, pp. 185–200, Dec 1994. ISSN: 1573-4862. doi: 10.1007/BF00742584. Disponível em: <https://doi.org/10.1007/BF00742584>.

[20] ROKHLIN, S. I., HEFETS, M., ROSEN, M. "An ultrasonic interface-wave method for predicting the strength of adhesive bonds", *Journal of Applied Physics*, v. 52, n. 4, pp. 2847–2851, 1981. doi: 10.1063/1.329016. Disponível em: <https://doi.org/10.1063/1.329016>.

[21] BELLMAN, R., KALABA, R. "Functional equations, wave propagation, and invariant imbedding", *J. Math. Mech.*, v. 8, pp. 683, 1959.

[22] BAIK, J.-M., THOMPSON, R. B. "Ultrasonic scattering from imperfect interfaces: A quasi-static model", *Journal of Nondestructive Evaluation*, v. 4, n. 3, pp. 177–196, 1984. ISSN: 1573-4862. doi: 10.1007/BF00566223. Disponível em: <http://dx.doi.org/10.1007/BF00566223>.

[23] PILARSKI, A., ROSE, J. L., DITRI, J., et al. "Lamb Wave Mode Selection for Increased Sensitivity to Interfacial Weaknesses of Adhesive Bonds". In: Thompson, D. O., Chimenti, D. E. (Eds.), *Review of Progress in Quantitative Nondestructive Evaluation: Volumes 12A and 12B*, pp. 1579–1585, Boston, MA, Springer US, 1993. ISBN: 978-1-4615-2848-7. doi: 10.1007/978-1-4615-2848-7_202. Disponível em: <http://dx.doi.org/10.1007/978-1-4615-2848-7_202>.

[24] GUO, N., CAWLEY, P. "The interaction of Lamb waves with delaminations in composite laminates", *The Journal of the Acoustical Society of America*, v. 94, n. 4, pp. 2240–2246, 1993. doi: 10.1121/1.407495. Disponível em: <http://dx.doi.org/10.1121/1.407495>.

[25] SINGHER, L., SEGAL, Y., SEGAL, E., et al. "Considerations in bond strength evaluation by ultrasonic guided waves", *The Journal of the Acoustical Society of America*, v. 96, n. 4, pp. 2497–2505, 1994. doi: 10.1121/1.410123. Disponível em: <http://dx.doi.org/10.1121/1.410123>.

[26] ALLEYNE, D., CAWLEY, P. "The interaction of Lamb waves with defects", *NDT and E International*, v. 29, n. 4, pp. 248–249, 1996.

[27] KARPUR, P., KUNDU, T., DITRI, J. J. "Adhesive Joint Evaluation Using Lamb Wave Modes with Appropriate Displacement, Stress, and Energy Distribution Profiles". In: Thompson, D. O., Chimenti, D. E. (Eds.), *Review of Progress in Quantitative Nondestructive Evaluation: Volume 18A–18B*, pp. 1533–1542, Boston, MA, Springer US, 1999. ISBN: 978-1-4615-4791-4. doi: 10.1007/978-1-4615-4791-4_197. Disponível em: <http://dx.doi.org/10.1007/978-1-4615-4791-4_197>.

[28] DIAMANTI, K., SOUTIS, C., HODGKINSON, J. "Non-destructive inspection of sandwich and repaired composite laminated structures", *Composites Science and Technology*, v. 65, n. 13, pp. 2059 – 2067, 2005. ISSN: 0266-3538. doi:

https://doi.org/10.1016/j.compscitech.2005.04.010. Disponível em: <http://www.sciencedirect.com/science/article/pii/S0266353805001004>.

[29] GRAFF, K. F. *Wave motion in elastic solids*. Courier Corporation, 2012.

[30] DIAMANTI, K., SOUTIS, C., HODGKINSON, J. "Lamb waves for the non-destructive inspection of monolithic and sandwich composite beams", *Composites Part A: Applied Science and Manufacturing*, v. 36, n. 2, pp. 189 – 195, 2005. ISSN: 1359-835X. doi: https://doi.org/10.1016/j.compositesa.2004.06.013. Disponível em: <http://www.sciencedirect.com/science/article/pii/S1359835X04001629>. 7th International Conference on the Deformation and Fracture of Composites (DFC-7).

[31] NASSR, A. A., EL-DAKHAKHNI, W. W. "Non-destructive evaluation of laminated composite plates using dielectrometry sensors", *Smart Materials and Structures*, v. 18, n. 5, pp. 055014, 2009. Disponível em: <http://stacks.iop.org/0964-1726/18/i=5/a=055014>.

[32] AMARO, A. M., REIS, P. N. B., DE MOURA, M. F. S. F., et al. "Damage detection on laminated composite materials using several NDT techniques", *Insight - Non-Destructive Testing and Condition Monitoring*, v. 54, n. 1, pp. 14–20, 2012. doi: doi:10.1784/insi.2012.54.1.14. Disponível em: <http://www.ingentaconnect.com/content/bindt/insight/2012/00000054/00000001/art00006>.

[33] REN, B., LISSENDEN, C. J. "Ultrasonic guided wave inspection of adhesive bonds between composite laminates", *International Journal of Adhesion and Adhesives*, v. 45, pp. 59 – 68, 2013. ISSN: 0143-7496. doi: https://doi.org/10.1016/j.ijadhadh.2013.04.001. Disponível em: <http://www.sciencedirect.com/science/article/pii/S0143749613000705>.

[34] KLIEBER, C., BRILL, T., CATHELINE, S., et al. "Visualization of Leaky Ultrasonic Lamb Wave Experiments in Multilayer Structures", *Physics Procedia*, v. 70, n. Supplement C, pp. 314 – 317, 2015. ISSN: 1875-3892. doi: https://doi.org/10.1016/j.phpro.2015.08.162. Disponível em: <http://www.sciencedirect.com/science/article/pii/S1875389215009037>. Proceedings of the 2015 ICU International Congress on Ultrasonics, Metz, France.

[35] LEIDERMAN, R., CASTELLO, D. "Scattering of ultrasonic waves by heterogeneous interfaces: Formulating the direct scattering problem as a least-squares problem", *The Journal of the Acoustical Society of America*, v. 135, n. 1, pp. 5–16, 2014. doi: 10.1121/1.4845615. Disponível em: <http://dx.doi.org/10.1121/1.4845615>.

[36] LEIDERMAN, R., FIGUEROA, J. C., BRAGA, A. M., et al. "Scattering of ultrasonic guided waves by heterogeneous interfaces in elastic multi-layered structures",

Wave Motion, v. 63, pp. 68 – 82, 2016. ISSN: 0165-2125. doi: https://doi.org/10.1016/j.wavemoti.2016.01.006. Disponível em: <http://www.sciencedirect.com/science/article/pii/S016521251600007X>.

[37] FUJIWARA, D., MORIMOTO, H. "An L_r-theorem of the Helmholtz decomposition of vector fields", *Journal of the Faculty of Science, the University of Tokyo. Sect. 1 A, Mathematics*, v. 24, pp. 685–700, 1977.

[38] SIMADER, C. G., SOHR, H., VARNHORN, W. "Necessary and sufficient conditions for the existence of Helmholtz decompositions in general domains", *ANNALI DELL'UNIVERSITA' DI FERRARA*, v. 60, n. 1, pp. 245–262, 2014. ISSN: 1827-1510. doi: 10.1007/s11565-013-0193-9. Disponível em: <http://dx.doi.org/10.1007/s11565-013-0193-9>.

[39] LEIDERMAN, R., BRAGA, A. M. B., BARBONE, P. E. "Scattering of ultrasonic waves by defective adhesion interfaces in submerged laminated plates", *The Journal of the Acoustical Society of America*, v. 118, n. 4, pp. 2154–2166, 2005. doi: 10.1121/1.2036147. Disponível em: <http://dx.doi.org/10.1121/1.2036147>.

[40] LEIDERMAN, R., BARBONE, P. E., BRAGA, A. M. B. "Reconstructing the adhesion stiffness distribution in a laminated elastic plate: Exact and approximate inverse scattering solutions", *The Journal of the Acoustical Society of America*, v. 122, n. 4, pp. 1906–1916, 2007. doi: 10.1121/1.2772212. Disponível em: <http://dx.doi.org/10.1121/1.2772212>.

[41] DRINKWATER, B. W., DWYER-JOYCE, R. S., ROBINSON, A. M. "The Use of Ultrasound to Investigate Rough Surface Contact Phenomena". In: Thompson, D. O., Chimenti, D. E. (Eds.), *Review of Progress in Quantitative Nondestructive Evaluation: Volume 18A–18B*, pp. 1455–1462, Boston, MA, Springer US, 1999. ISBN: 978-1-4615-4791-4. doi: 10.1007/978-1-4615-4791-4_187. Disponível em: <http://dx.doi.org/10.1007/978-1-4615-4791-4_187>.

[42] GOLUB, M. V. "Propagation of elastic waves in layered composites with microdefect concentration zones and their simulation with spring boundary conditions", *Acoustical Physics*, v. 56, n. 6, pp. 848–855, 2010. ISSN: 1562-6865. doi: 10.1134/S1063771010060084. Disponível em: <http://dx.doi.org/10.1134/S1063771010060084>.

[43] GOLUB, M. V., BOSTRÖM, A. "Interface damage modeled by spring boundary conditions for in-plane elastic waves", *Wave Motion*, v. 48, n. 2, pp. 105 – 115, 2011. ISSN: 0165-2125. doi: https://doi.org/10.1016/j.wavemoti.2010.09.003. Disponível em: <http://www.sciencedirect.com/science/article/pii/S0165212510000818>.

[44] ROKHLIN, S. I., HUANG, W. "Ultrasonic wave interaction with a thin anisotropic layer between two anisotropic solids: Exact and asymptotic-boundary-condition methods", *The Journal of the Acoustical Society of America*, v. 92, n. 3, pp. 1729–1742, 1992. doi: 10.1121/1.403912. Disponível em: <http://dx.doi.org/10.1121/1.403912>.

[45] RAJABI, M., HASHEMINEJAD, S. M. "Acoustic resonance scattering from a multilayered cylindrical shell with imperfect bonding", *Ultrasonics*, v. 49, n. 8, pp. 682 – 695, 2009. ISSN: 0041-624X. doi: https://doi.org/10.1016/j.ultras.2009.05.007. Disponível em: <http://www.sciencedirect.com/science/article/pii/S0041624X09000626>.

[46] ZAKHAROV, D. D. "High order approximate low frequency theory of elastic anisotropic lining and coating", *The Journal of the Acoustical Society of America*, v. 119, n. 4, pp. 1961–1970, 2006. doi: 10.1121/1.2169922. Disponível em: <http://dx.doi.org/10.1121/1.2169922>.

[47] AN, Z., WANG, X., DENG, M., et al. "A nonlinear spring model for an interface between two solids", *Wave Motion*, v. 50, n. 2, pp. 295 – 309, 2013. ISSN: 0165-2125. doi: https://doi.org/10.1016/j.wavemoti.2012.09.004. Disponível em: <http://www.sciencedirect.com/science/article/pii/S0165212512001278>.

[48] ANGEL, Y. C., ACHENBACH, J. D. "Reflection and Transmission of Elastic Waves by a Periodic Array of Cracks", *Journal of Applied Mechanics*, v. 52, pp. 33–41, 1984.

[49] AULD, B. A. *Acoustic fields and waves in solids*. Krieger Publishing Company, 1990.

[50] WILLIAMS, J. H., NAYEB-HASHEMI, H., LEE, S. S. "Ultrasonic attenuation and velocity in AS/3501-6 graphite fiber composite", *Journal of Nondestructive Evaluation*, v. 1, n. 2, pp. 137–148, Jun 1980. ISSN: 1573-4862. doi: 10.1007/BF00566121. Disponível em: <https://doi.org/10.1007/BF00566121>.

[51] TIAN, J., WANG, Q., GUO, Q., et al. "Casing integrity evaluation in deep well with extreme heavy mud in Tarim Basin", *SPE EUROPEC/EAGE Annual Conference and Exhibition*, 2011.